CEDAR-GPP: spatiotemporally upscaled estimates of gross primary productivity incorporating CO_2 fertilization

Yanghui Kang[1,2], Max Gaber[1,3], Maoya Bassiouni[1,2], Xinchen Lu[1,2], Trevor F. Keenan[1,2]

[1] Department of Environmental Science, Policy, and Management, University of California, Berkeley, Berkely, CA 94720, USA

[2] Climate and Ecosystem Sciences Division, Lawrence Berkeley National Laboratory, Berkeley, CA 94720, USA

[3] Department of Geosciences and Natural Resource Management, University of Copenhagen, Copenhagen, 1350, Denmark.

Correspondence: Yanghui Kang (yanghuikang@berkeley.edu)

Trevor Keenan (trevorkeenan@berkeley.edu)

Abstract: Gross primary productivity (GPP) is the largest carbon flux in the Earth system, playing a crucial role in removing atmospheric carbon dioxide and providing the sugars and starches needed for ecosystem metabolism. Despite the importance of GPP, however, existing estimates present significant uncertainties and discrepancies. A key issue is the underrepresentation of the CO_2 fertilization effect, a major factor contributing to the increased terrestrial carbon sink over recent decades. This omission could potentially bias our understanding of ecosystem responses to climate change.

Here, we introduce CEDAR-GPP, the first global upscaled GPP product that incorporates the direct CO_2 fertilization effect on photosynthesis. Our product is comprised of monthly GPP estimates and their uncertainty at 0.05° resolution from 1982 to 2020, generated using a comprehensive set of eddy covariance measurements, multi-source satellite observations, climate variables, and machine learning models. Importantly, we used both theoretical and data-driven approaches to incorporate the direct CO_2 effects. Our machine learning models effectively predicted monthly GPP ($R^2 \sim 0.74$), the mean seasonal cycles ($R^2 \sim 0.79$), and spatial variabilities ($R^2 \sim 0.67$). Incorporation of the direct CO_2 effects substantially improved the models' ability to estimate long-term GPP trends across global flux sites. While the global patterns of annual mean GPP, seasonality, and interannual variability generally aligned with existing satellite-based products, CEDAR-GPP demonstrated higher long-term trends globally after incorporating CO_2 fertilization, particularly in the tropics, reflecting a strong temperature control on direct CO_2 effects. CEDAR-GPP offers a comprehensive representation of GPP temporal and spatial dynamics, providing valuable insights into ecosystem-climate interactions.

1. Introduction

Terrestrial ecosystem photosynthesis, known as Gross Primary Productivity (GPP), is the primary source of food and energy for the Earth system and human society. Through photosynthesis, terrestrial ecosystems also mitigate climate change, by removing thirty percent of anthropogenic carbon emissions from the atmosphere each year (Friedlingstein et al., 2023). However, due to the lack of direct measurements at the global scale, our understanding of photosynthesis and its spatiotemporal dynamics is limited, leading to considerable disagreements among various GPP estimates (Anav et al., 2015; O'Sullivan et al., 2020; Smith et al., 2016; Yang et al., 2022). Addressing these uncertainties is crucial for improving the predictability of ecosystem dynamics under climate change (Friedlingstein et al., 2014).

Over the past three decades, global networks of eddy covariance flux towers collected *in situ* carbon flux measurements that allow for accurate estimates of GPP, providing valuable insights into photosynthesis dynamics under various environmental conditions (Baldocchi, 2020; Beer et al., 2010). To quantify and understand GPP at scales and locations beyond the ~ 1km2 flux tower footprints, machine learning has been employed with gridded satellite and climate datasets to upscale site-based measurements and produce wall-to-wall GPP maps (Yang et al., 2007; Xiao et al., 2008; Jung et al., 2011; Tramontana et al., 2016; Joiner and Yoshida, 2020; Zeng et al., 2020; Dannenberg et al., 2023). This approach provides important observational constraints of global carbon dynamics, complementing process-based and semi-process-based modeling such as Terrestrial biosphere models or the Light Use Efficiency (LUE) models (Beer et al., 2010; Jung et al., 2017; Schwalm et al., 2017; Gampe et al., 2021).

Effective machine learning upscaling depends on a complete set of input predictors that fully explain GPP dynamics. Upscaled datasets have primarily relied on satellite-observed greenness indicators, such as vegetation indexes (VIs), Leaf Area Index (LAI), the fraction of absorbed photosynthetically active radiation (fAPAR), which effectively capture canopy-level GPP dynamics related to leaf area changes (Tramontana et al., 2016; Ryu et al., 2019; Joiner and Yoshida, 2020). However, important aspects of leaf-level physiology, such as those controlled by climate factors, are often omitted in major upscaled datasets, preventing accurate characterization of GPP responses to climate change (Stocker et al., 2019; Bloomfield et al., 2023). In particular, none of the previous upscaled datasets have considered the direct effect of atmospheric CO_2 on leaf-level photosynthesis, which is a key factor contributing to at least half of the enhanced land carbon sink observed over the past decades (Keenan et al., 2016; Keenan and Williams, 2018; Walker et al., 2021; Ruehr et al., 2023). This omission can lead to incorrect inference regarding long term trends in various components of the terrestrial carbon cycle (De Kauwe et al., 2016).

Multiple independent lines of evidence from atmospheric inversion (Wenzel et al., 2016), atmospheric $^{13}C/^{12}C$ measurements (Keeling et al., 2017), ice core records of carbonylsulfide (Campbell et al., 2017), glucose isotopomers (Ehlers et al., 2015), as well as free-air CO_2 enrichment experiments (FACE) (Walker et al., 2021), suggest a widespread positive effect of elevated atmospheric CO_2 on GPP from site to global scales. Increasing CO_2 *directly* stimulates the biochemical rate of leaf-level photosynthesis, leading to an increase in net carbon assimilation and leaf area, which enhances canopy-level GPP. Furthermore, high CO_2 concentration is expected to reduce stomatal conductance and increase water use efficiency, indirectly enhancing photosynthesis under water-limited conditions (De Kauwe et al., 2013; Keenan et al., 2013). The direct biochemical effect has been found to dominate GPP responses to CO_2, from both theoretical and observational analyses (Haverd et al., 2020; Chen et al., 2022).

Satellite-based estimates have shown an increasing global GPP trend in the past few decades largely attributable to CO_2-induced increases in LAI (De Kauwe et al., 2016; Zhu et al., 2016; Chen et al., 2019; Piao et al., 2020). However, previous upscaled GPP datasets, as well as most LUE models such as the MODIS GPP product, have failed to consider the direct CO_2 effects on leaf-level biochemical processes (Jung et al., 2020; Zheng et al., 2020). Consequently, these products likely underestimated the long-term trend of global GPP, leading to large discrepancies when compared to process-based models, which typically consider leaf-level CO_2 effects (Anav et al., 2015; De Kauwe et al., 2016; O'Sullivan et al., 2020). Notably, recent improvements in LUE models have included the CO_2 response and show improved long-term changes in GPP globally (Zheng et al., 2020), yet, this important mechanism is still missing in GPP products upscaled from *in situ* eddy covariance flux measurements.

To improve the quantification of GPP spatial and temporal dynamics and provide a robust representation of long-term dynamics in global photosynthesis, we developed the CEDAR-GPP[1] data product. CEDAR-GPP was upscaled from global eddy covariance carbon flux measurements using machine learning along with a broad range of multi-source satellite observations and climate variables. In addition to incorporating direct CO_2 fertilization effects on photosynthesis, we also

[1] CEDAR stands for upsCaling Ecosystem Dynamics with ARtificial inteligence

account for indirect effects via greenness indicators, and include novel satellite datasets such as solar-induced fluorescence (SIF), Land Surface Temperature (LST) and soil moisture to explain variability under environmental stresses. We provide monthly GPP estimations and associated uncertainties at 0.05° resolution derived from ten model setups. These setups differ by the temporal range depending on satellite data availability, the method for incorporating the direct CO_2 fertilization effects, and the partitioning approach used to derive GPP from eddy covariance measurements. Short-term GPP datasets were from 2001 to 2020, primarily based on data derived from MODIS satellites, and long-term datasets spaned 1982 to 2020 using combined Advanced Very High Resolution Radiometer (AVHRR) and MODIS data. We used two approaches to incorporate the direct CO_2 fertilization effects including direct prescription with eco-evolutionary theory and machine learning inference from the eddy-covariance data. Additionally, we provided a baseline configuration that did not incorporate the direct CO_2 effects. Uncertainties in GPP estimation were quantified using bootstrapped model ensembles. We evaluate the machine learning models' skills in predicting monthly GPP, seasonality, interannual variability, and trend against eddy covariance measurements, and compare the CEDAR-GPP spatial and temporal variability to existing satellite-based GPP estimates.

2. Data and Methods

2.1 Eddy covariance data

We obtained monthly eddy covariance GPP measurements from 2001 to 2020 from FLUXNET2015 (Pastorello et al., 2020), AmeriFlux FLUXNET (https://ameriflux.lbl.gov/data/flux-data-products/), and ICOS Warm Winter 2020 (Warm Winter 2020 Team and ICOS Ecosystem Thematic Centre., 2022) datasets. All data were processed with the ONEFLUX pipeline (Pastorello et al., 2020). Following previous upscaling efforts (Tramontana et al., 2016), we selected monthly GPP data that had at least 80% of high-quality hourly or half-hourly data for temporal aggregation. We further excluded large negative GPP values, setting a cutoff of -1 $gCm^{-2}d^{-1}$. We utilized GPP estimates from both the night-time (GPP_REF_NT_VUT) and day-time (GPP_REF_DT_VUT) partitioning approaches and trained separate machine learning models for each. We classified flux tower sites according to the primary C3 and C4 plant categories reported in metadata and related publications when available and used a C4 plant percentage map (Still et al.,

2003) otherwise. Our analysis encompassed 233 sites, predominately located in North America, Western Europe, and Australia (Figure 1). In total, our dataset included roughly 18000 site-months.

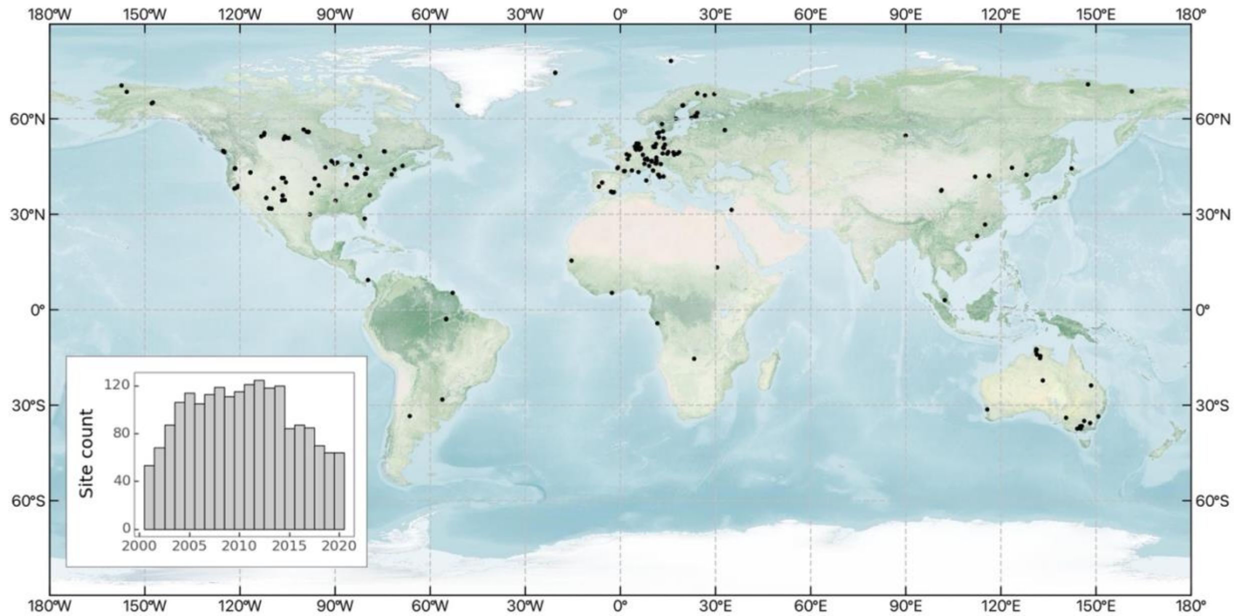

Figure 1. Global distribution of eddy covariance sites used to generate the CEDAR-GPP product. The inset displays the annual count of sites.

2.2 Global input datasets

We compiled an extensive set of covariates from gridded climate reanalysis data, multi-source satellite datasets including optical, thermal, and microwave observations, as well as categorical information on land cover, climate zone, and C3/C4 classification. The datasets that we compiled offer comprehensive information about GPP dynamics and its responses to climatic variabilities and stresses. Table 1 lists the inputs datasets and associated variables used to generate CEDAR-GPP.

Table 1. Datasets and input variables used to generate the CEDAR GPP product. For a list of selected variables used in different model setups, please refer to Table S1.

Category	Dataset	Temporal coverage	Spatial resolution	Temporal resolution	Variables	Reference
Climate	ERA5-Land Monthly Averaged data	1950 – present	0.1°	Monthly	Air temperature; vapor pressure deficit, Precipitation, Air and skin temperature, surface downwelling solar radiation, Potential evaporation	(Sabater, 2019)

	ESRA Global Monitoring Laboratory Atmospheric Carbon Dioxide	1976 – present	-	Monthly	Atmospheric CO_2 concentration averaged from Mauna Loa, Hawaii, US and South Pole, Antarctica	(Thoning et al., 2021)
Satellite-based datasets	MODIS Nadir BRDF-adjusted reflectance (MCD43C4)	2000 – present	0.05°	Daily	Surface reflectance b1 – b7, Vegetation indices (NIRv, NDVI, kNDVI, EVI, GCI, NDWI), percent snow	(Schaaf and Wang, 2015)
	MODIS Terra and Aqua LAI/fPAR (MCD15A3H, MOD15A2H)	2000 – present	500m	4-day, 8-day	LAI, fPAR	(Myneni et al., 2015a, b)
	MODIS Terra and Aqua LST (MYD11A1, MOD11A1)	2000 – present	1 km	Daily	Daytime LST Nighttime LST	(Wan et al., 2015b, a)
	BESS_Rad	2000 – 2020	0.05°	Daily	PAR, diffuse PAR, downwelling solar radiation	(Ryu et al., 2018)
	Continuous-SIF (from OCO-2 and MODIS)	2000 – 2020	0.05°	4-day	all-sky daily average SIF	(Zhang, 2021)
	ESA CCI Soil Moisture Combined Passive and Active	1979 – 2021	0.25°	Daily	Surface soil moisture	(Gruber et al., 2019)
	GIMMS LAI4g	1982 – 2021	0.0833°	Half-month	LAI	(Cao et al., 2023)
	GIMMS NDVI4g	1982 – 2021	0.0833 °	Half-month	NDVI	(Li et al., 2023)
Static categorical datasets	MODIS Land Cover (MCD12Q1)	Average status used between 2001 and 2020	500m	-	Plant function types	(Friedl and Sulla-Menashe, 2019)
	Koppen-Geiger Climate Classification	present	1 km	-	Koppen-Geiger climate classes	(Beck et al., 2018)
	C4 percentage map	present	1°	-	Percentage of C4 plants	(Still et al., 2003, 2009)

2.2.1 Climate variables

We obtained air temperature, vapor pressure deficit, precipitation, potential evapotranspiration, and skin temperature from the EAR5-Land reanalysis dataset (Sabater, 2019) (Table 1; Table S1). We applied a three-month lag to precipitation, to reflect the memory of soil moisture and represent the root zone water availability. Averaged monthly atmospheric CO_2 concentrations were calculated as an average of records from the Mauna Loa Observatory and South Pole Observation stations, retrieved from NOAA's Earth System Research Laboratory (Thoning et al., 2021).

2.2.2 Satellite datasets

We assembled a broad collection of satellite-based observations of vegetation greenness and structure, LST, solar radiation, solar-induced fluorescence (SIF), and soil moisture (Table 1, Table S1).

Three MODIS products were used: surface reflectance, LAI/fAPAR, and LST. Surface reflectance from optical to infrared bands (band 1 to 7) was sourced from the MODIS Nadir BRDF-adjusted reflectance (NBAR) daily dataset (MCD43C4) (Schaaf and Wang, 2015). From this, we derived several vegetation indexes, including NIRv (Badgley et al., 2019), kNDVI (Camps-Valls et al., 2021), NDVI, Enhanced Vegetation Index (EVI), Normalized Difference Water Index (NDWI) (Gao, 1996), and a green chlorophyll index (CIgreen) (Gitelson, 2003). We also used snow percentages from the NBAR dataset. We used the 4-day LAI and fPAR composite derived from Terra and Aqua satellites (MCD15A3H) (Myneni et al., 2015a; Yan et al., 2016a, b) from July 2002 onwards and the MODIS 8-day LAI and fPAR dataset from Terra only (MOD15A2H) prior to July 2002 (Myneni et al., 2015b). We used day-time and night-time LST from the Aqua satellite (MYD11A1) (Wan et al., 2015b), with the Terra-based LST product (MOD11A1) used after July 2002 (Wan et al., 2015a). Terra LST was bias-corrected with the differences in the mean seasonal cycles between Aqua and Terra following Walther et al. (2021).

We used the PKU GIMMS NDVI4g dataset (Li et al., 2023) and PKU GIMMS LAI4g (Cao et al., 2023) datasets available from 1982 to 2020. PKU GIMMS NDVI4g is a harmonized time series that includes AVHRR-based NDVI from 1982 to 2003 (with biases and corrections mitigated through inter-calibration with Landsat surface reflectance images) and MODIS NDVI from 2004 onward. PKU GIMMS LAI4g consisted of AVHRR-based LAI from 1982 to 2003 (generated using machine learning models trained with Landsat-based LAI data and NDVI4g) and MODIS BNU LAI from 2004 onwards (Yuan et al., 2011).

We utilized photosynthetically active radiation (PAR), diffusive PAR, and shortwave downwelling radiation from the BESS_Rad dataset (Ryu et al., 2018). We also obtained the continuous-SIF (CSIF) dataset (Zhang et al., 2018; Zhang, 2021) produced by a machine learning algorithm trained using OCO-2 SIF observations and MODIS surface reflectance. We also obtained surface soil moisture from the ESA CCI soil moisture combined passive and active product (Dorigo et al., 2017; Gruber et al., 2019).

2.2.3 Other categorical datasets

We used plant functional type (PFT) information derived from the MODIS Land Cover product (MCD12Q1) (Friedl and Sulla-Menashe, 2019). We followed the International Geosphere-Biosphere Program classification scheme but merged several similar categories to maximize the amount of eddy covariance sites/observations available for each category. Closed shrublands and open shrublands are combined into a shrubland category. Woody savannas and savannas are combined into savannas. We generated a static PFT map by taking the mode of the MODIS land cover time series between 2001 – 2020 at each pixel to mitigate uncertainties from misclassification in the MODIS dataset. Nevertheless, changes in vegetation structure induced by land use and land cover change are reflected in the dynamics surface reflectance and LAI/fAPAR datasets we used. We used the Koppen-Geiger main climate groups (tropical, arid, temperate, cold, and polar) (Beck et al., 2018). We also utilized a C4 plant percentage map to account for different photosynthetic pathways when incorporating CO_2 fertilization (Still et al., 2003, 2009).

2.2.4 Data preprocessing

We implemented a three-step preprocessing strategy for the satellite datasets: 1) quality control, 2) gap-filling, and 3) spatial and temporal aggregation. In the first step, we selected high-quality data based on the quality control flags of the satellite products when available. For the MODIS NBAR dataset (MCD43C3), we used data with 75% or more high-resolution NBAR pixels retrieved with full inversions for each band. For MODIS LST, we selected the best quality data from the quality control bitmask as well as data where retrieved values had an average emissivity error of no more than 0.02. For MODIS LAI/fAPAR, we used retrievals from the main algorithm with or without saturation. We used all available data in ESA-CCI soil moisture due to the presence of substantial data gaps. In the gap-filling step, missing values in satellite datasets were temporally filled at the native temporal resolution, following a two-step protocol adapted from Walther et al (2021). Short temporal gaps were first filled with medians from a moving window, and the remaining gaps were filled with the mean seasonal cycle. For datasets with a high temporal resolution, including MODIS NBAR (daily), LAI/fPAR (4-day), BESS (4-day), CSIF (4-day), ESA-CCI (daily), temporal gaps no longer than 5 days (8 days for 4-day resolution products) were filled with medians of 15-day moving windows in the first step. An exception is MODIS LST (daily), for which we used a shorter moving window of 9 days due to rapid changes in surface temperature. GIMMS LAI4g and NDVI4g data were only filled with mean seasonal cycle due to their low temporal resolution (bi-monthly). In the last processing step, all the datasets were aggregated to a monthly time step and 0.05-degree spatial resolution.

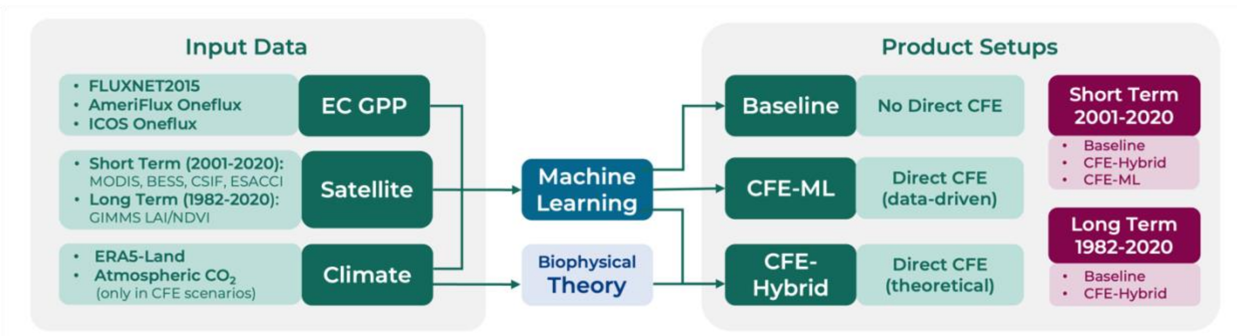

Figure 2. Schematic overview of the CEDAR-GPP model setups.

2.3 Machine learning upscaling

2.3.1 CEDAR-GPP model setups

We trained machine learning model with eddy covariance GPP measurements as targets and climate/satellite variables as input features. We created ten model setups to produce ten different global monthly GPP datasets (Figure 2; Table 2). The model setups were characterized by the temporal range of input datasets used, the configuration of CO2 fertilization effects, and the partitioning approach used to derive the GPP from eddy covariance measurements.

We provided a short-term (ST) configuration producing GPP estimates from 2001 to 2020, and a long-term (LT) configuration spanning 1982 to 2020. Each temporal configuration uses a different set of input variables depending on their temporal availability. Inputs for the short-term configuration included MODIS, CSIF, BESS PAR, ESA-CCI soil moisture, ERA5-Land, as well as PFT and Koppen Climate zone as categorical variables with one-hot encoding. The long-term used GIMMS NDVI4g and LAI4g data, ERA5-land, PFT and Koppen climate. ESA CCI soil moisture datasets were excluded from the long-term model setups due to concerns about the product quality in the early years when the number and quality of microwave satellite data were limited (Dorigo et al., 2015). A detailed list of input features for each setup is provided in Table S1.

Regarding the direct CO_2 fertilization effects (CFE), we established a "Baseline" configuration that did not incorporate these effects, a "CFE-Hybrid" configuration that incorporated the effects via eco-evolutionary theory, and a "CFE-ML" configuration that inferred direct effects from eddy covariance data using machine learning. Detailed information about these approaches is provided in Section 2.4.2. Furthermore, separate models were trained for GPP target variables from the night-time (NT) and daytime (DT) partitioning approaches.

Table 2 lists the characteristics of ten model setups. Note due to the limited availability of eddy covariance observations before 2001, we did not apply the CFE-ML approach to the long-term setups, as the machine learning inferred CO2 fertilization effects cannot be robustly extrapolate GPP back to 1982.

Table 2. Specifications of the CEDAR-GPP model setups.

Model Setup Name	Temporal range	Direct CO_2 Fertilization Effects		GPP Partitioning Method
		Configuration	Method	
ST_Baseline_NT	Short-term (ST) 2001 – 2020	Baseline	Not incorporated	Night-time (NT)
ST_Baseline_DT				Day-time (DT)
ST_CFE-Hybrid_NT		CFE-Hybrid	Theoretical	NT
ST_CFE-Hybrid_DT				DT
ST_CFE-ML_NT		CFE-ML	Data-driven	NT
ST_CFE-ML_DT				DT
LT_Baseline_NT	Long-term (LT) 1982 – 2020	Baseline	Not incorporated	NT
LT_Baseline_DT				DT
LT_CFE-Hybrid_NT		CFE-Hybrid	Theoretical	NT
LT_CFE-Hybrid_DT				DT

2.3.2 CO_2 fertilization effect

We established three configurations considering the direct CO_2 fertilization effects on photosynthesis. In the baseline configuration, we trained machine learning models with eddy covariance GPP measurements, input climate and satellite features, but excluding CO_2 concentration. As such, the models only include indirect CO_2 effects from the satellite-based proxies of vegetation greenness and structure and do not consider the direct effect of CO_2 on light use efficiency. Our baseline model is therefore directly comparable to other satellite-derived GPP products that only account for indirect CO2 effects (ref FLUXCOM, FLUXSAT, MODIS).

In the CFE-ML configuration, we added trained monthly CO_2 concentration into the feature set in addition to those incorporated in the baseline models. Thus, models inferred the functional relationship between GPP and CO_2 from the eddy covariance data, encompassing both CO_2 fertilization pathways – direct effects on LUE and indirect effects from the satellite-based proxies of vegetation greenness and structure.

In the CFE-Hybrid configuration, we applied biophysical theory to estimate the response of LUE to elevated CO_2. First, we estimated a reference GPP, where LUE is not affected by any increase in atmospheric CO_2, by applying the CFE-ML model with a constant atmospheric CO_2 concentration equal to the 2001 level while keeping all other variables temporally dynamic. Then, the impacts of CO_2 on LUE were prescribed onto the reference GPP estimates using a theoretical CO_2 sensitivity function of LUE according to eco-evolutionary theories (Supplementary Text S1). The theoretical CO_2 sensitivity function represents a CO_2 sensitivity that is equivalent to that of the electron-transport-limited (light-limited) photosynthetic rate. When light is limited, elevated CO_2 suppresses photorespiration leading to increased photosynthesis at a lower rate than when photosynthesis is limited by CO_2 (Lloyd and Farquhar, 1996; Smith and Keenan, 2020). Thus, the CFE-Hybrid scenario provides a conservative estimation of the direct CO_2 effects on LUE. Note that the theoretical sensitivity function describes the fractional change in LUE due to direct CO_2 effects relative to a reference period (i.e. 2001). Therefore, we used the CFE-ML model to establish this reference GPP by fixing the CO_2 effects to the 2001 level, rather than simply using the GPP from the Baseline model in which the direct CO_2 effects were not clearly represented.

For both CFE-ML and CFE-Hybrid scenarios, we made another conservative assumption that C4 plants do not benefit from elevated CO_2, despite potential increases in photosynthesis during water-limited conditions due to enhanced WUE. Data from flux tower sites dominated by C4 plants were removed from our training set, so the machine learning models inferred CO_2 fertilization only from flux tower sites dominated by C3 plants. When applying models globally, we assumed the reference GPP values (with constant atmospheric CO_2 concentration equal to the 2001 level) to represent C4 plants, and GPP estimates from CFE-ML or CFE-Hybrid models wereapplied in proportion to the percentage of C3 plants in a grid cell.

2.3.3 Machine learning model training and validation

We employed the state-of-the-art XGBoost machine learning model, known for its high accuracy in regression problems across various domains, including environmental and ecological predictions (Chen and Guestrin, 2016; Kang et al., 2020; Berdugo et al., 2022). XGBoost is a scalable and parallelized implementation of the gradient boosting technique that iteratively trains an ensemble of decision trees, with each iteration targeting to minimize the residuals from the last iteration. A notable merit of XGBoost is its ability to make prediction in the presence of missing values, a common issue in remote sensing datasets.

We used five-fold cross-validation for model evaluation. Training data was randomly split into five groups (folds), with each fold held out for testing while the rest four folds were used for model training. We imposed two restrictions on fold splitting: each flux site was entirely assigned to a fold to test model performance over unseen locations; the random sampling was stratified based on PFT to ensure coverage of the full range of PFTs in both training and testing. Within each training set, we performed a randomized search using three-fold cross-validation to determine the optimal hyperparameter set, to reduce the risk of overfitting and improve the robustness of the evaluation.

We assessed the models' ability to capture the temporal and spatial characteristics of GPP, including monthly variabilities, mean seasonal cycles, monthly anomalies, cross-site variability. Model performance was assessed separately for each model setup (Table 2) and summarized by PFT and Koppen climate zone. Mean seasonal cycles were calculated as the mean monthly GPP over the site observation period, and monthly anomalies were the residuals of monthly GPP after subtracting mean seasonal cycles. Monthly GPP averaged over years for each site was used to assess cross-site variability. Goodness-of-fit metrics include RMSE, bias, and coefficient of determination (R^2, equivalent to NSE Nash–Sutcliffe model efficiency coefficient).

To evaluate the models' ability to capture long-term GPP trends, we aggregated the monthly GPP to annual values for sites with at least 5 years of observations following Chen et al. (2022). GPP anomalies were computed by subtracting the multi-year mean GPP from the annual GPP for each site. Anomalies were aggregated across site to achieve a single multi-site GPP anomaly per year. We used the Sen slope and Mann-Kendall test to examine the GPP trends from 2002 to 2019, excluding 2001 and 2020 due to the limited number of available sites.

2.3.4 Product generation and uncertainty quantification

In the CEDAR-GPP product, we generated a GPP dataset for each of the ten model setups, by applying the model to global gridded datasets within the corresponding temporal range (Table 2). GPP datasets were named after the corresponding model setups. For each model setup, we first generated 30 sample set using bootstrapping, which were then used to train an ensemble of 30

XGBoost models. The bootstrapping was performed at the site level, and each bootstrapped sample set contained around 140 to 150 unique sites, 17000 to 19000 site months covering all PFTs. The relative composition of sites in each PFT was consistent with the full dataset. The 30 models trained with bootstrapped samples generated an ensemble of 30 GPP values. We provided the ensemble GPP mean and standard deviation from each of the ten model setups.

2.4 Product inter-comparison

We compared the global spatial and temporal patterns of CEDAR-GPP with other major satellite-based GPP products including three machine learning upscaled and two LUE-based datasets. We obtained two FLUXCOM products (Jung et al., 2020), the latest version of FLUXCOM-RS (FLUXCOM-RSv006) available from 2001 to 2020 based on remote sensing (MODIS collection 6) datasets only, as well as the FLUXCOM-RS+METEO ensemble available between 1979 to 2018 and based on the climatology of remote sensing observations and ERA5 forcings (hereafter FLUXCOM-ERA5). We used FluxSat (Joiner and Yoshida, 2020), available from 2001 to 2019, which is an upscaled dataset based on MODIS NBAR surface reflectance and PAR from Modern-Era Retrospective analysis for Research and Applications 2 (MERRA-2). Importantly, FluxSat does not incorporate climate forcings. We used the MODIS GPP product (MOD17) available since 2001, which was generated based on MODIS fAPAR and LUE as a function of air temperature and vapor pressure deficit but not atmospheric CO_2 concentration (Running et al., 2015). We also used the rEC-LUE products, available from 1982 to 2018 and based on a revised LUE model that incorporated the effect of atmospheric CO_2 concentration and the fraction of diffuse PAR on LUE in addition to air temperature and vapor pressure deficit (Zheng et al., 2020). All datasets were resampled to 0.1 ° spatial resolution, and a common mask for the vegetated land area was applied. We evaluated global mean annual GPP, mean seasonal cycle, interannual variability, and trend among different datasets, comparing them over a common time period determined by their data availability. Global total GPP was computed by scaling the global average GPP flux with the global land area (122.4 million km2) following Jung et al. (2020). Mean seasonal cycle was defined as above (Sec 2.3.3). We used the standard deviation of annual GPP to indicate the magnitude of interannual variability, the Sen slope to indicate GPP annual trend and the Mann-Kendall test for the statistical significance of trends.

3. Results

3.1 Evaluation of model performance

3.1.1 Overall performance

The short-term and long-term models explained approximately 74% and 68%, respectively, of the variation in eddy covariance estimated monthly GPP across global sites (Figure 3a). The long-term models consistently yielded lower performance than the short-term models, likely due to differences in the satellite remote sensing datasets used, as the short-term models benefited from a richer information including surface reflectance from individual bands, LST, CSIF, as well as soil moisture, while the long-term model only exploited NDVI and LAI. The models with different CFE scenarios and target GPP variables had similar performance on predicting monthly GPP (Figure 3b, Table 3, Table S2). All models exhibited minimal bias less than 0.15.

Model performance in terms of the different temporal and spatial characteristics of monthly GPP was variable (Figure 3c-h). The models were most successful at predicting mean seasonal cycles, with the short-term and long-term models explaining around 79% and 72% of the variability, respectively (Figure 3c-d). The short-term and long-term models captured 66% and 54% , respectively of the spatial variabilities of multi-year mean GPP across global sites (i.e., cross-site variability) (Figure 3g-h). However, all models predicted monthly anomalies across the sites, with R^2 values below 0.11 (Figure 3e-f). The CFE-ML and CFE-Hybrid models showed slightly higher accuracy than the Baseline model across all temporal and spatial characteristics.

Table 3. Machine learning model performance for five CEDAR-GPP setups based on NT GPP (Table 2). Results of DT setups can be found in Table S2.

Model Setup Name	Monthly			Mean seasonal cycles			Monthly anomalies			Cross-site		
	RMSE	Bias	R^2	RMSE	Bias	R^2	RMSE	Bias	R^2	RMSE	Bias	R^2
ST_Baseline_NT	1.96	-0.05	0.74	1.57	0.02	0.79	1.22	0.00	0.11	1.11	0.03	0.66
ST_CFE-ML_NT	1.95	-0.05	0.74	1.56	0.02	0.80	1.22	0.00	0.12	1.10	0.03	0.67
ST_CFE-Hybrid_NT	1.96	-0.05	0.74	1.57	0.03	0.79	1.23	0.00	0.12	1.10	0.04	0.67
LT_Baseline_NT	2.18	-0.10	0.68	1.82	0.01	0.72	1.26	0.00	0.06	1.29	0.03	0.54
LT_CFE-Hybrid_NT	2.16	-0.11	0.69	1.79	0.01	0.73	1.25	0.00	0.07	1.27	0.03	0.56

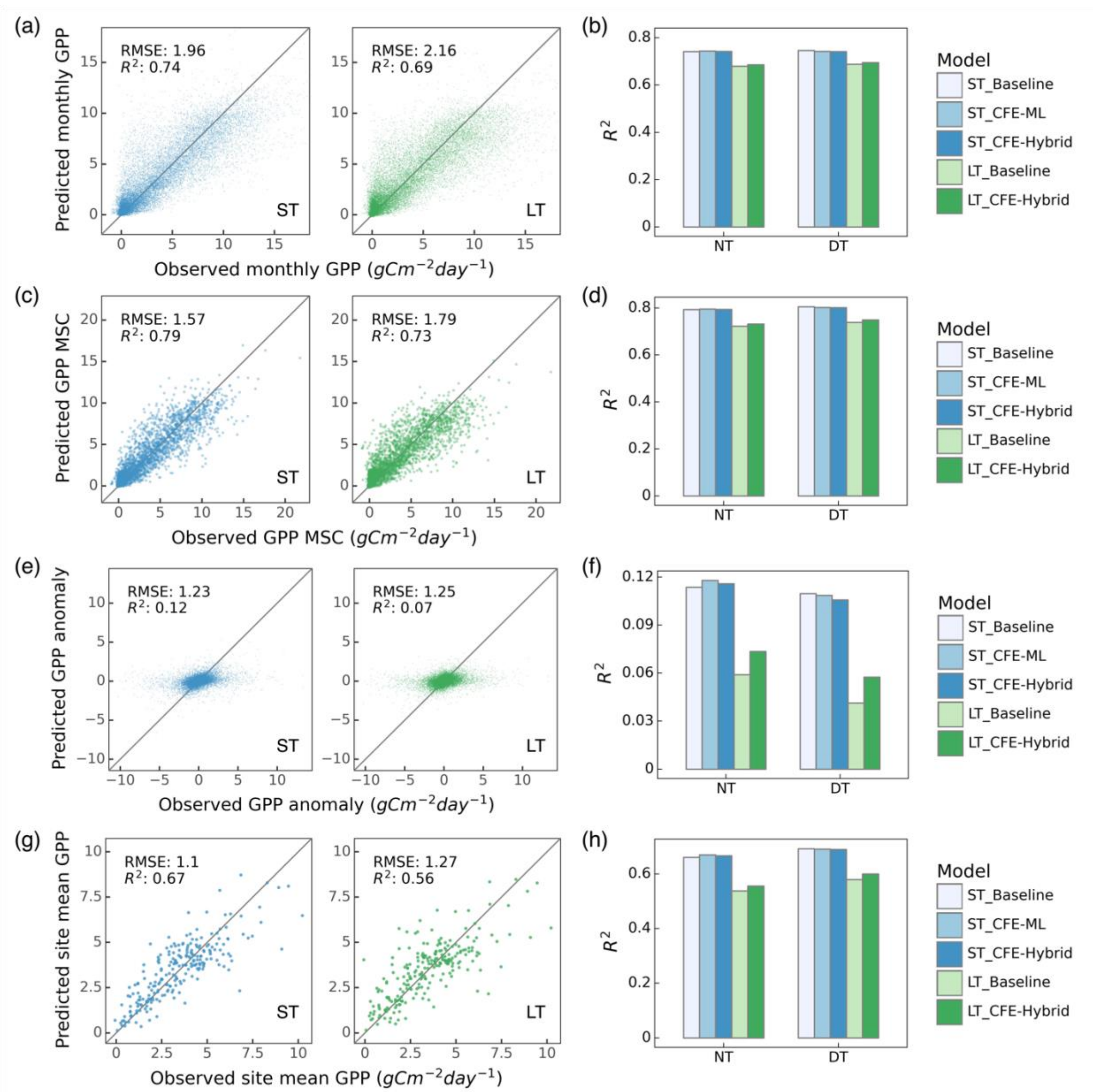

Figure 3. Machine learning model performance in predicting monthly GPP and its spatial and temporal variability. Scatter plots illustrated relationships between model predictions and observations for monthly GPP (a), mean seasonal cycles (MSC (c), monthly anomaly (e), and cross-site variability (g) for ST_CFE-Hybrid_NT (left, blue) and LT_CFE-Hybrid_NT (right, green) models. Corresponding bar plots show the R^2 values for all ten model setups in predicting monthly GPP (b), MSC (d), monthly anomaly (f), and cross-site variability (h).

3.1.2 Performance by biome and climate zone

The predictive ability of our models varied across different PFTs and Koppen climate zones (Figure 4). Here we present results from the CFE-Hybrid models and note that patterns for the other CFE configurations were similar.

Model performance in terms of monthly GPP was highest for forests with distinct seasonality, including deciduous broadleaf forests, mixed forests, and evergreen needleleaf forests, with R^2 values above 0.78. Model accuracies were also high for savannas, and grasslands, followed by croplands and wetlands, with R^2 values between 0.57 and 0.74. Model accuracies were lowest in evergreen broadleaf forests and shrublands, with R^2 values as low as 0.14. Across climate zones, models achieved the highest accuracy in predicting monthly GPP in cold and tropical climate zones with R^2 values between 0.64 and 0.80. The short-term models had lowest performance in polar regions with an R^2 value around 0.42 and the long-term model had the lowest performance in arid regions with an R^2 value of 0.25.

Model performance in terms of mean seasonal cycles across PFTs and climate zones followed patterns for monthly GPP, while disparities emerged for performance in terms of GPP anomaly and cross-site variability (Figure 4). The short-term model showed the highest predictive power in explaining monthly anomalies in arid regions with an R^2 value of 0.49, where savanna and shrublands sites are primarily located. Model performance in all other climate zones was significantly lower with R^2 values below 0.2, and as low as 0.07 in temperate regions. Besides, the short-term model demonstrated good performance in capturing anomalies in deciduous broadleaf forests. The long-term model's relative performance between PFTs and climate zones was mostly consistent with that of the short-term model, with lower accuracy in shrublands when compared to the short-term model.

Model performance in terms of cross-site variability demonstrated highest accuracy in savannas, grasslands, evergreen needleleaf forests, and evergreen broadleaf forests ($R^2 > 0.36$) and lowest accuracy in deciduous broadleaf forests, mixed forests, and croplands ($R^2 < 0.20$). The short-term model additionally showed good performance in shrublands and wetlands ($R^2 > 0.36$), whereas the long-term model failed to capture any variability for shrublands. In terms of climate zones, models were most successful at explaining the variabilities across tropical and cold climate zones ($R^2 > 0.46$), the short-term model was least successful across polar regions, with a R^2 value of 0.29, and the long-term model had low performance for both polar and arid regions with R^2 values below 0.15.

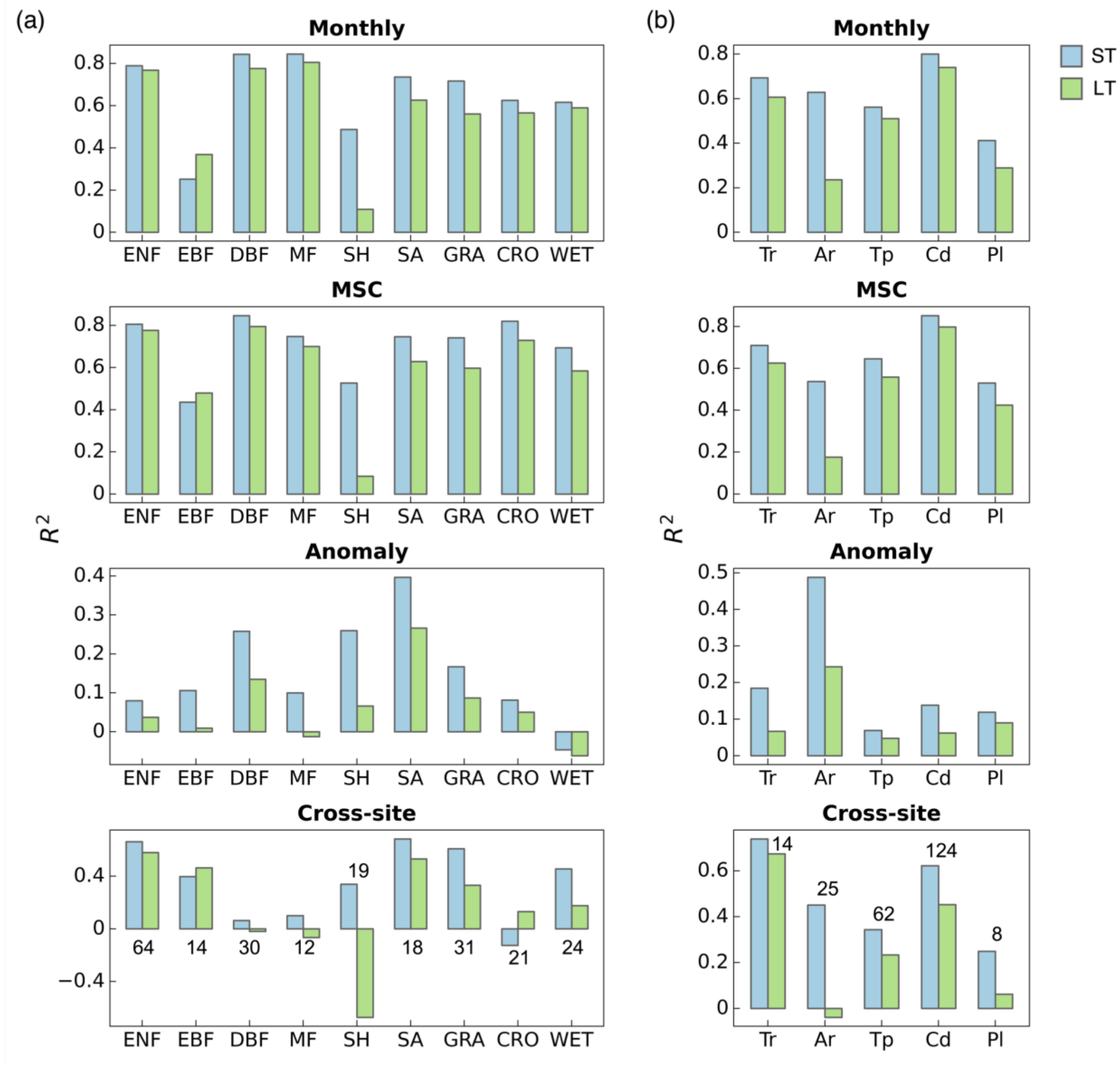

Figure 4. Performance of the ST_Baseline_NT (blue) and LT_Baseline_NT (green) models on GPP spatiotemporal estimation by plant functional types (a) and climate zones (b). The cross-site panels included the number of sites within each category. ENF: evergreen needleleaf forest, EBF: evergreen broadleaf forest, DBF: deciduous broadleaf forest, MF: mixed forest, SH: shrubland, SA: savanna, GRA: grassland, CRO: cropland, WET: wetland. Tr: tropical, Ar: arid, Tp: temperate, Cd: cold, Pl: polar.

3.1.3 Prediction of long-term trends

Eddy covariance measured GPP presented a substantial increasing trend in GPP across flux sites between 2002 and 2019 (Figure 5a). The observed GPP from the night-time partitioning approach indicated an overall trend of 7.7 $gCm^{-2}year^{-2}$. In contrast, the ST_ Baseline_NT model predicted a more modest trend of 2.7 gCm^{-2}year^{-2}, primarily reflecting the indirect CO_2 effect manifested through the growth of LAI. Both the ST_CFE-ML_NT and ST_CFE-hybrid_NT models predicted much higher trends of 5.5 and 4.3 gCm^{-2}year$^{-2,}$ respectively, aligning more closely to eddy covariance observations.

Across all model setups, the CFE-ML and CFE-hybrid models consistently outperformed the Baseline models in predicting GPP trends in global eddy covariance towers (Figure 6b) and all trends were statistically significant ($p < 0.05$). Notably, we found a considerably higher trend in eddy covariance GPP measurements derived from the day-time versus night-time partitioning approach. The predicted trends of different model setups between the partitioning approaches were similar despite a smaller trend predicted by the ST_CFE-ML_DT model compared to the corresponding NT model (Figure 6b).

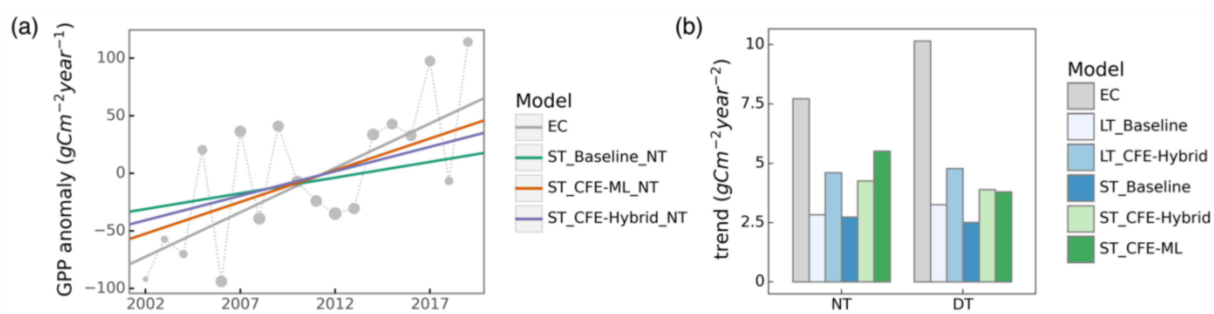

Figure 5. Comparison of observed and predicted GPP trends across eddy covariance flux towers. (a) Aggregated annual GPP anomaly from 2002 to 2019 and trend lines from eddy covariance (EC) measurements, and three CFE model setups (short-term, night-time partitioning). Size of the grey circle markers is proportional to the number of sites. (b) Annual trends from eddy covariance measurements and ten CEDAR-GPP model setups.

3.2 Evaluation of GPP spatial and temporal dynamics

In this section, we present comparisons between CEDAR-GPP datasets and other upscaled or LUE-based datasets regarding the mean annual GPP (Section 3.2.1), GPP seasonality (Section 3.2.2), interannual variability (Section 3.2.3), and annual trends (Section 3.2.4). CEDAR-GPP model setups generally showed similar patterns in mean annual GPP, seasonality, and interannual variability, therefore, in corresponding sections, we present the CFE-Hybrid model setups as representative examples for comparisons with other independent datasets, unless otherwise stated. Supplementary figures include comparisons involving all CEDAR-GPP.

3.2.1 Mean annual GPP

Global patterns of mean annual GPP were generally consistent among CEDAR-GPP model setups, FLUXCOM, FLUXSAT, MODIS, and rEC-LUE, with few noticeable regional differences (Figure 6, Figure S1). Differences among CEDAR-GPP model setups were minimal and only evident between the NT and DT setups in the tropics (Figure 6b-c, Figure S1). CEDAR-GPP short-term datasets showed highest consistency with FLUXSAT in terms of mean annual GPP magnitudes (2001 – 2018) and latitudinal variations, although FLUXSAT presented slightly higher GPP values in the tropics compared to CEDAR-GPP (Figure 6b). Mean annual GPP magnitude for FLUXCOM-RS006 and MODIS tended to be lower globally than CEDAR-GPP and FLUXSAT, with the most pronounced differences observed in the tropical areas. Among the long-term datasets (CEDAR-GPP LT, FLUXCOM-ERA5, and rEC-LUE), mean annual GPP (1982 – 2018) exhibited greater disparities in the northern mid-latitudes than in the tropics and southern hemisphere (Figure 6c). CEDAR-GPP aligned more closely with FLUXCOM-ERA5 than with rEC-LUE, with the latter showing lower annual mean GPP globally, particularly between 20ºN to 50º N.

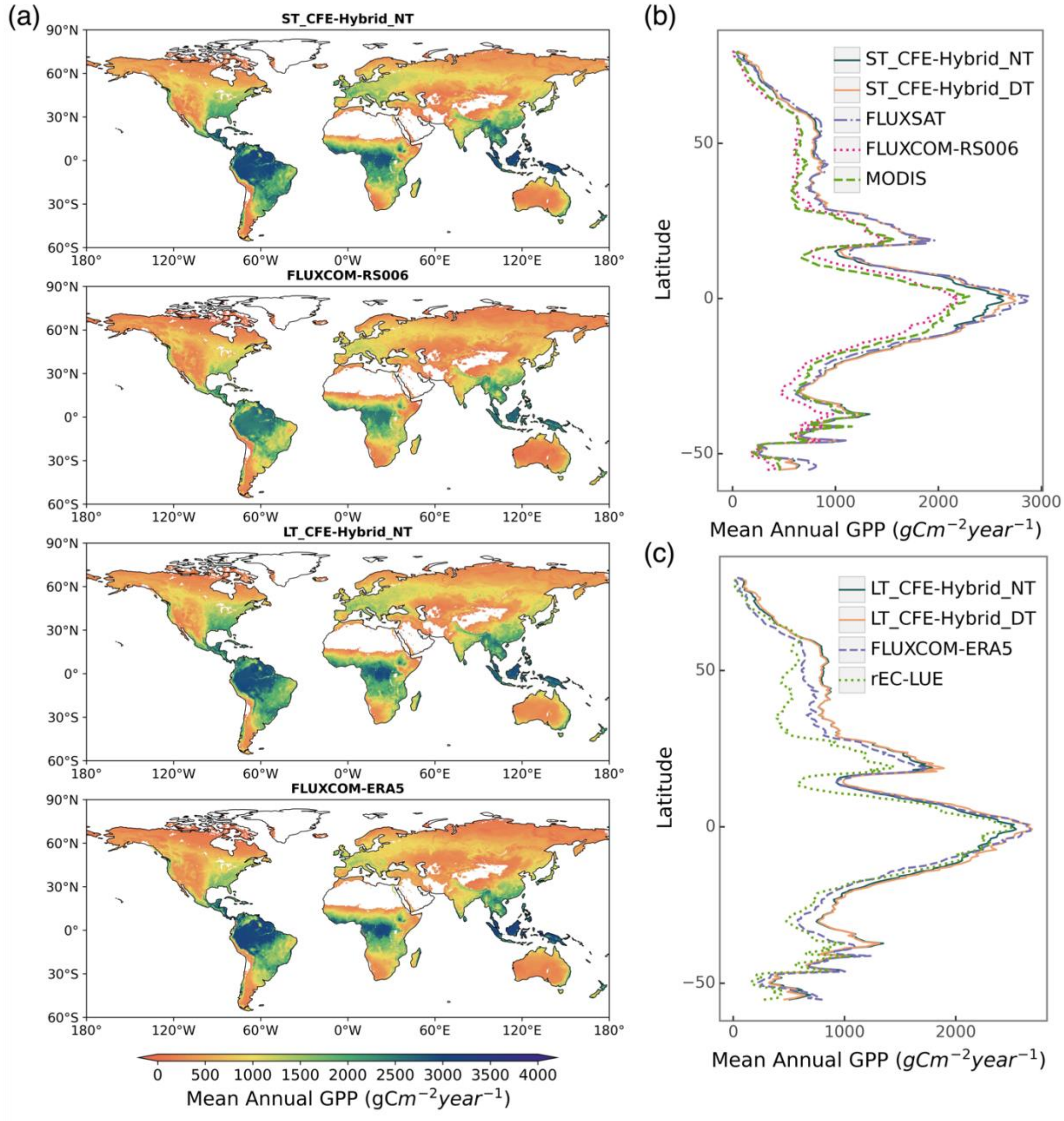

Figure 6. Global distributions of mean annual GPP from CEDAR-GPP and other machine learning upscaled and LUE-based reference datasets. (a) Global patterns of mean annual GPP from ST_CFE-Hybrid_NT, FLUXCOM-RS006, LT_CFE-Hybrid_NT, and FLUXCOM-ERA5. (b) Latitudinal distributions of mean annual GPP (2001 – 2018) from short-term datasets (ST_CFE-Hybrid_NT, ST_CFE-Hybrid_DT, FLUXSAT, FLUXCOM-RS006, and MODIS. (c) Latitudinal distributions of mean annual GPP (1982 – 2018) from long-term datasets (LT_CFE-Hybrid_NT, LT_CFE-Hybrid_DT, FLUXCOM-ERA5, and rEC-LUE.

3.2.2 Seasonal variability

CEDAR-GPP and other machine learning upscaled and LUE-based GPP datasets agreed on seasonal variabilities (average between 2001 and 2018) at the global scale, characterized by a peak in GPP in July and a nadir between December and January (Figure 7). At the global scale, CEDAR-GPP was most closely aligned with FLUXSAT in GPP seasonal magnitude and amplitude, while both FLUXCOM and MODIS displayed a relatively less pronounced magnitude.

In the northern hemisphere (20ºN - 90ºN), all GPP datasets agreed in seasonal GPP variation, despite variances in the magnitude of peak GPP. In the southern hemisphere (20ºS - 60ºS), all datasets exhibited their lowest GPP during June and July, and highest GPP from December to January. However, the seasonal amplitude of GPP was greatest for FLUXCOM-ERA5, followed by CEDAR-GPP and FLUXSAT, and substantially smaller for FLUXCOM-RS006 and MODIS GPP. In the tropics (20ºN - 20ºS), differences between datasets were the strongest, where seasonal variation is not as prominent compared to other regions. CEDAR-GPP, FLUXSAT, and FLUXCOM-ERA5 each showed two GPP peaks, occurring in March-April and September-October. Although FLUXCOM-RS006 had a similar seasonal pattern, its GPP magnitude was markedly smaller. Interestingly, MODIS showed an inverse season pattern with a small peak from June to August.

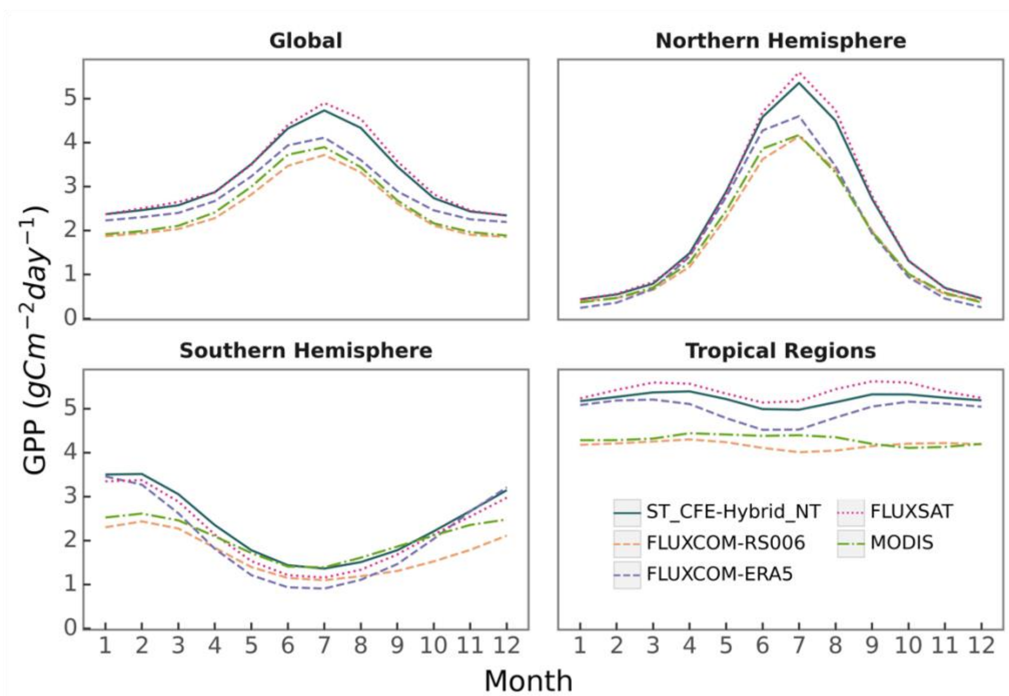

Figure 7. Comparison of GPP mean seasonal cycle between different datasets on a global scale, and specifically withi the Northern Hemisphere (20ºN - 90ºN), Southern

Hemisphere (20ºS - 60ºS), and Tropical regions (20ºN - 20ºS). Monthly means were averaged from 2001 to 2018 for all datasets.

3.2.3 Interannual variability

We found distinct spatial patterns in GPP interannual variability between upscaled and LUE-based datasets and a high level of agreement within each category, with the exception of FLUXCOM-ERA5, which showed minimal interannual variability globally (Figure 8). All datasets agreed on the presence of GPP interannual variability hotspots in eastern and southern South America, central North America, southern Africa, and western Australia. These hotspots primarily corresponded to arid and semi-arid areas characterized by grasslands, shrubs, and croplands (Figure 9). CEDAR-GPP was highly consistent with FLUXSAT, and both datasets also displayed relatively high interannual variability in the dry subhumid areas of Europe, predominately covered by croplands. FLUXCOM-RS006 mirrored the relative spatial patterns of CEDAR-GPP and FLUXSAT, albeit at lower magnitudes. The LUE-based datasets (MODIS and rEC-LUE) predicted a much higher interannual variability than the upscaled datasets in the tropical areas, particularly in evergreen broadleaf forests and woody savannas (Figure 8, Figure 9). These datasets also depicted slightly higher interannual variability for other types of forests, including evergreen needleleaf forests and deciduous broadleaf forests, compared to the upscaled datasets.

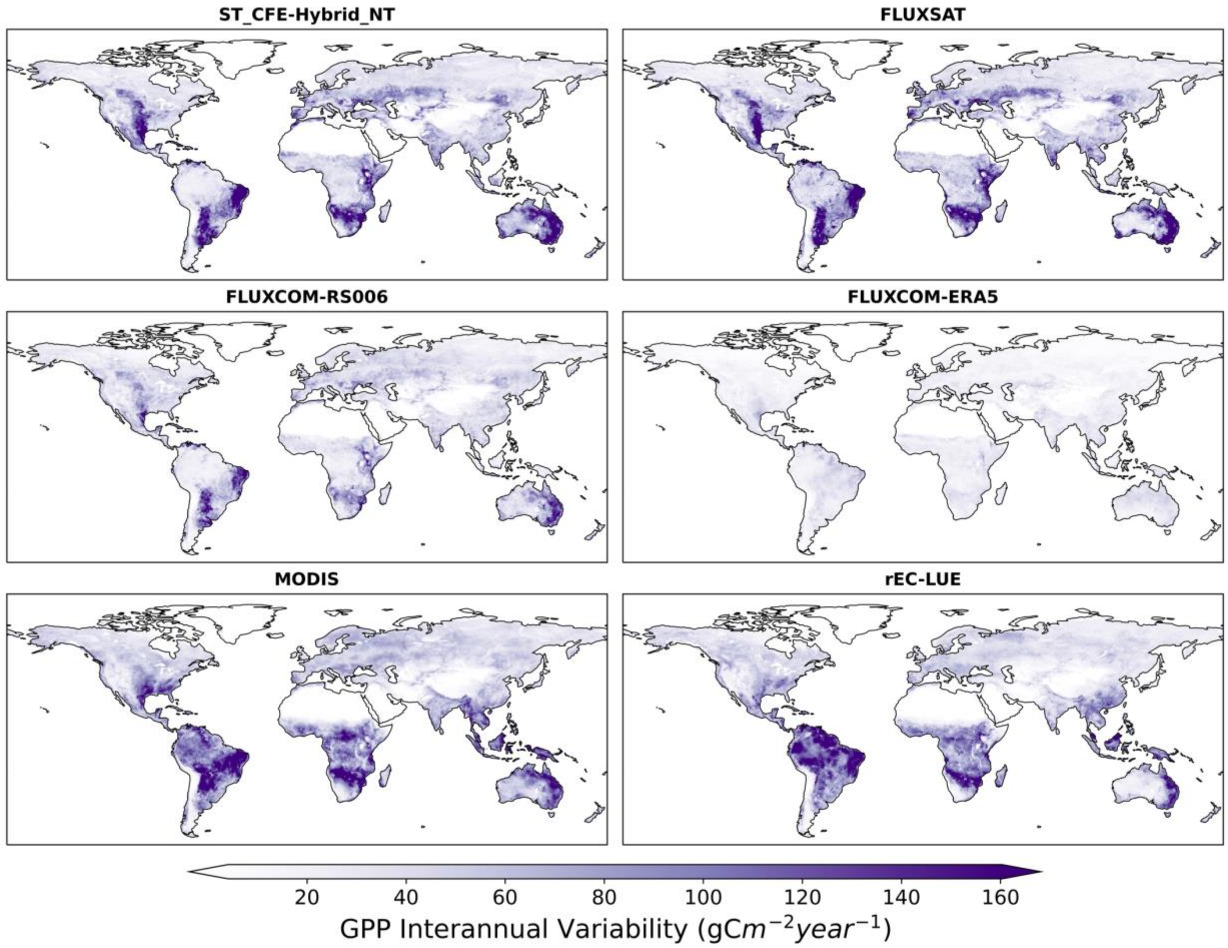

Figure 8. Spatial patterns of GPP interannual variability extracted over 2001 to 2018 for CEDAR-GPP (ST_CFE-Hybrid_NT), FLUXSAT, FLUXCOM-RS006, MODIS, FLUXCOM-ERA5, and rEC-LUE.

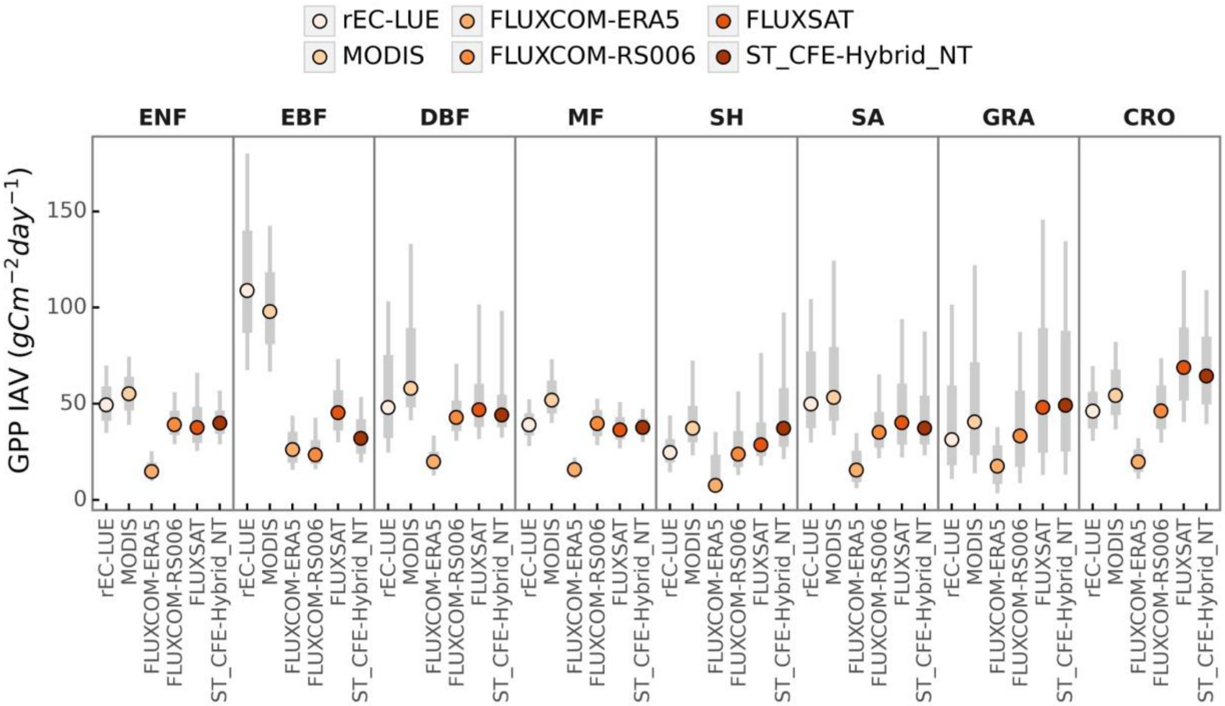

Figure 9. Comparison of GPP interannual variability (IAV across global datasets by PFT. Colored dots represent the median IAV, thicker grey bars indicate the 25% to 75% percentiles of IAV distributions, and thinner grey bards show the 10% to 90% percentiles.

3.2.4 Trends

Differences in annual GPP trends among CEDAR-GPP model setups and other upscaled and LUE-based datasets mainly reflected the variability in the representation of CO_2 fertilization effects (Figure 10, Figure S4). From 2001 to 2018, the CEDAR-GPP Baseline model setups showed spatial variations in GPP trends consistent with the other upscaled datasets without direct CO_2 fertilization effects, including FLUXSAT and FLUXCOM-RS. In these datasets, substantial increases were seen in southeastern China and India, western Europe, and part of North and South America. These increases were largely associated with rising LAI due to land use changes and indirect CO_2 fertilization effects, as identified by previous studies (Zhu et al., 2016; Chen et al., 2019). Although MODIS, which also does not include a direct CO_2 fertilization effect, generally agreed with these increasing trends, it also showed a declining GPP in the tropical Amazon and a stronger positive trend in central South America. After incorporating the direct CO_2 fertilization effects, both the CFE-Hybrid and CFE-ML setups predicted positive trends in tropical forests, an observation absent in all other datasets. Furthermore, the CFE-Hybrid and CFE-ML models also revealed increasing

GPP in temperate and boreal forests of North America and Eurasia. Notably, all datasets agreed on a pronounced GPP decrease in eastern Brazil.

From 2001 to 2018, a positive trend in global annual GPP was uniformly detected by all, albeit with varying magnitudes (Figure 11a-b). The ST_Baseline_NT model predicted a GPP growth rate of 0.35 Pg C per year, aligning with FLUXCOM-RS, but lower than FLUXSAT (0.51 Pg C yr^{-1}) and MODIS (0.39Pg C yr^{-1}) (Figure 11b). The CFE-hybrid models estimated a notably faster GPP growth at 0.58 Pg C per year. The CFE-ML models predicted the highest trends, up to 0.76 from the ST_CFE-ML_NT model and 0.59 from the ST_CFE-ML_DT model. Also, a higher variance was observed among ensemble members in the ST_CFE-ML setups compared to the ST_Baseline and ST_CFE-Hybrid models.

From 1982 to 2018, the LT_Baseline models identified increasing GPP trends in large areas of Europe, East and South Asia, as well as Northern Amazon (Figure 10b). The patterns from LT_CFE-Hybrid models aligned closely with the LT_Baseline models but exhibited a stronger positive trend in global tropical areas as well as Eurasian boreal forests. In contrast, FLUXCOM-ERA5 showed overall negative trends in the tropics, despite a small magnitude. Lastly, rEC-LUE agreed with positive GPP trends identified in CEDAR-GPP in the extratropical areas, but predicted a pronounced negative trend in the tropics. At the global scale, all the CEDAR-GPP long-term models predicted an increasing global GPP trend (Figure 11d). The LT_Baseline models showed a trend of 0.13 to 0.15 Pg C $year^{-2}$, while the LT_CFE-Hybrid setups doubled that rate. rEC-LUE showed a two-phased pattern with a strong increase in GPP from 1982 to 2000 (0.54 Pg C $year^{-2}$), followed by a decreasing trend after 2001 (-0.20 Pg C $year^{-2}$) (Figure S5). This resulted in an overall positive change at a rate comparable to that of the Baseline model. FLUXCOM-ERA5 exhibited a small negative trend.

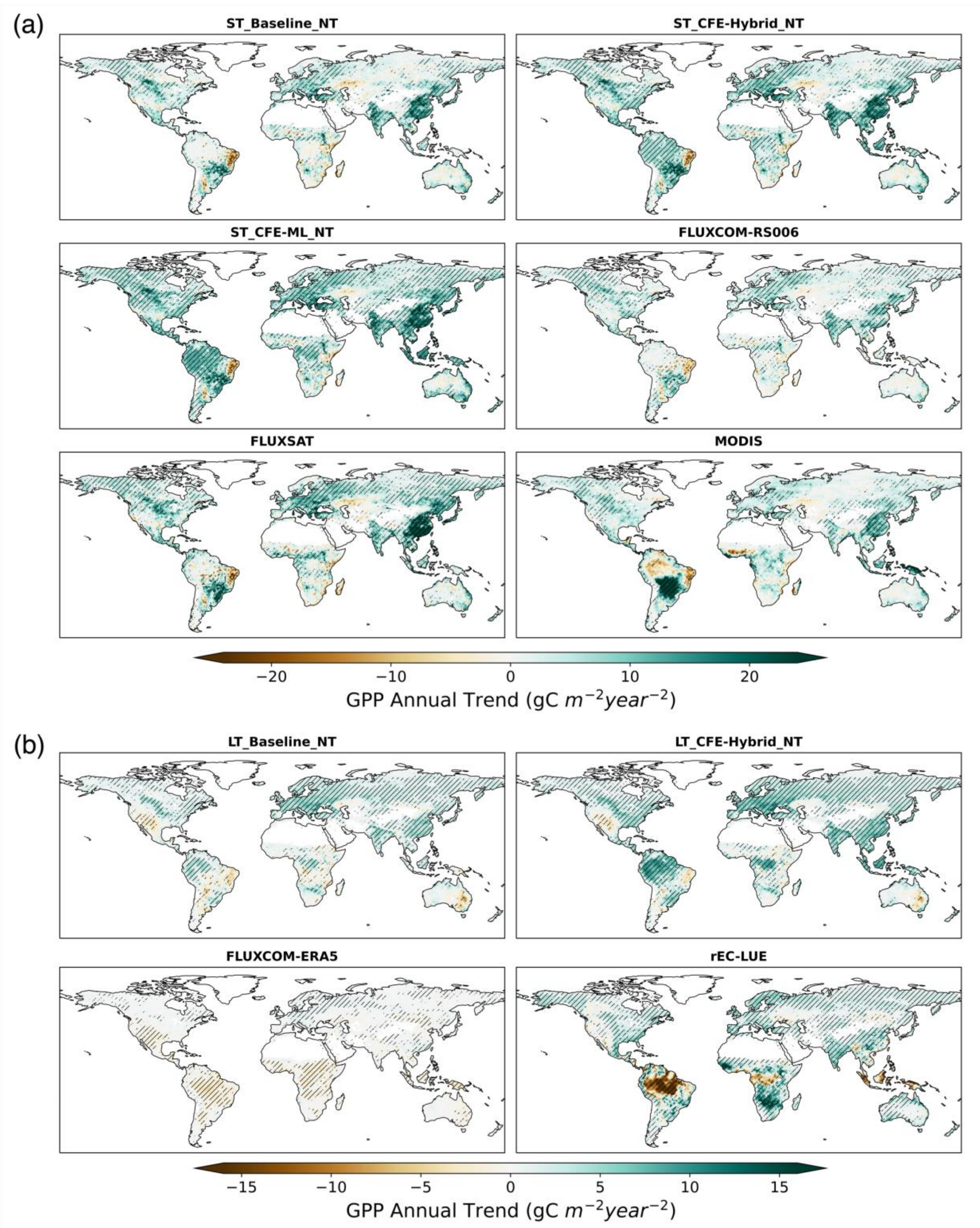

Figure 10. Annual GPP trend over 2001 – 2018 for short-term CEDAR-GPP, FLUXCOM-RS006, FLUXSAT, and MODIS datasets (a) and over 1982 – 2018 for long-term CEDAR-GPP, FLUXCOM-ERA5 and rEC-LUE datasets (b). Hatched

areas indicate the GPP trend that is statistically significant at $p < 0.05$ level under the Mann-Kendal test.

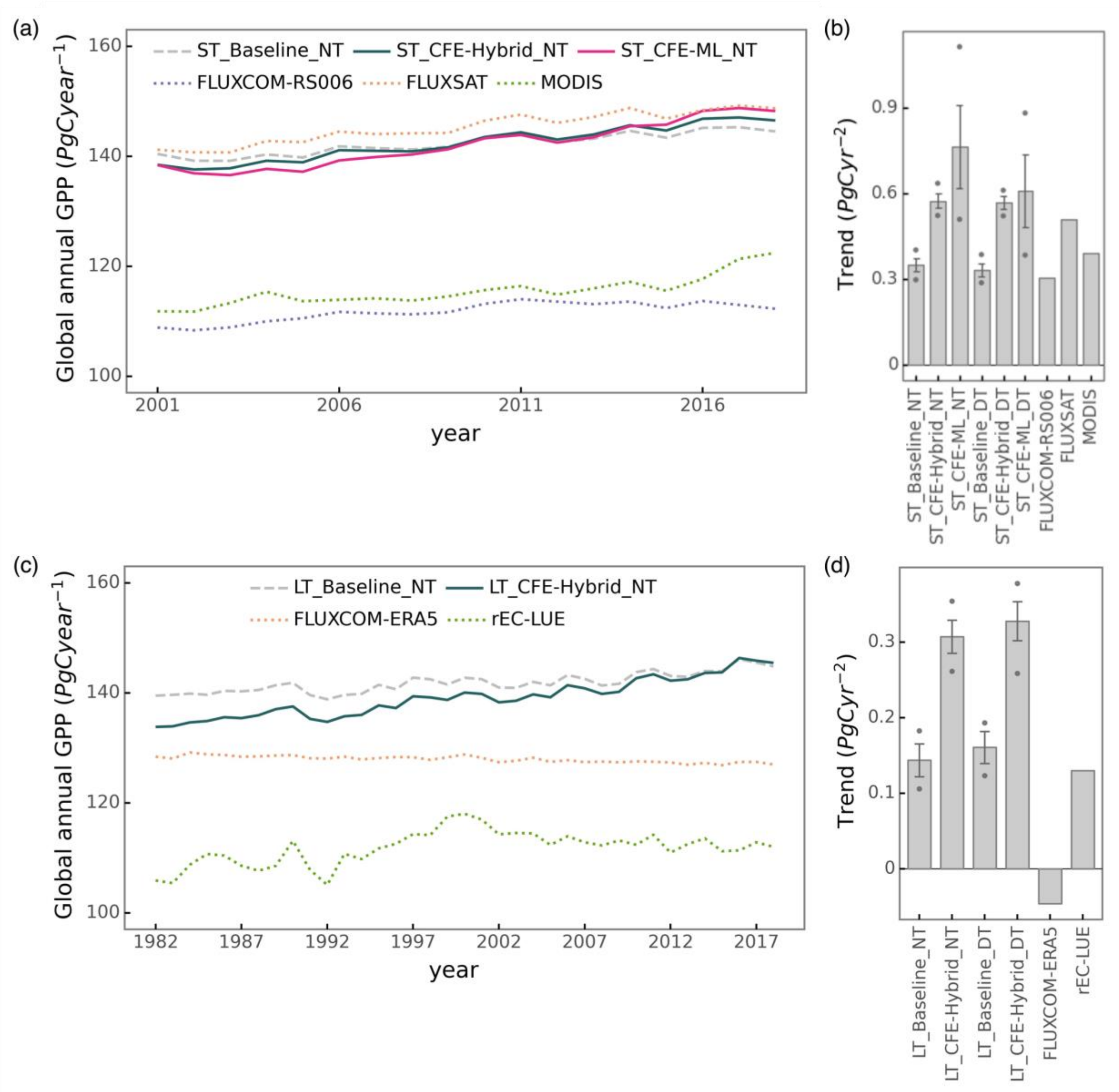

Figure 11. Global annual GPP variations (a) and trends (b) over 2001 to 2018 for short-term CEDAR-GPP, FLUXCOM-RS006, FLUXSAT, and MODIS datasets Global annual GPP variations (c) and trends (d) over 1982 to 2018 for long-term for long-term CEDAR-GPP, FLUXCOM-ERA5, and rEC-LUE datasets. Error bars in (b) and (d) represent the 25% to 75% percentile from the model ensembles of CEDAR-GPP. Dots in (b) and (d) indicate the minimum and maximum from the model ensembles of CEDAR-GPP.

3.3 GPP estimation uncertainties

We analyzed the spread between the 30 model ensemble members in CEDAR-GPP as an indicator of uncertainties in GPP estimations. The spatial pattern of uncertainty in estimating annual mean GPP largely resembled that of the mean map (Figure 12, Figure 6a). The largest model spread was found in highly productive tropical forests, and this uncertainty decreased in temperate and cold areas (Figure 12a). Tropical ecosystems, with a mean annual GPP between 1000 to 3500 $PgCyr^{-1}$, only exhibited a 2% and 6% variation within the model ensemble (Figure 12b). Ecosystems in the temperate and cold climates had a smaller annual GPP and proportionally small uncertainties up to 6%. However, ecosystems in Arid and Polar climates, despite their similarly low GPP, showed higher model uncertainty, reaching 10% to 40% of the ensemble mean. The estimation uncertainty of GPP trends was generally below 15% to 20% in the CEDAR-GPP datasets under the ST_Baseline and ST_CFE-Hybrid setups (Figure 12c). However, in the ST_CFE-ML setup, the estimation increased substantially, with model spread reaching up to 40% in tropical areas. Notably, the long-term models showed a higher uncertainty compared to the short-term models.

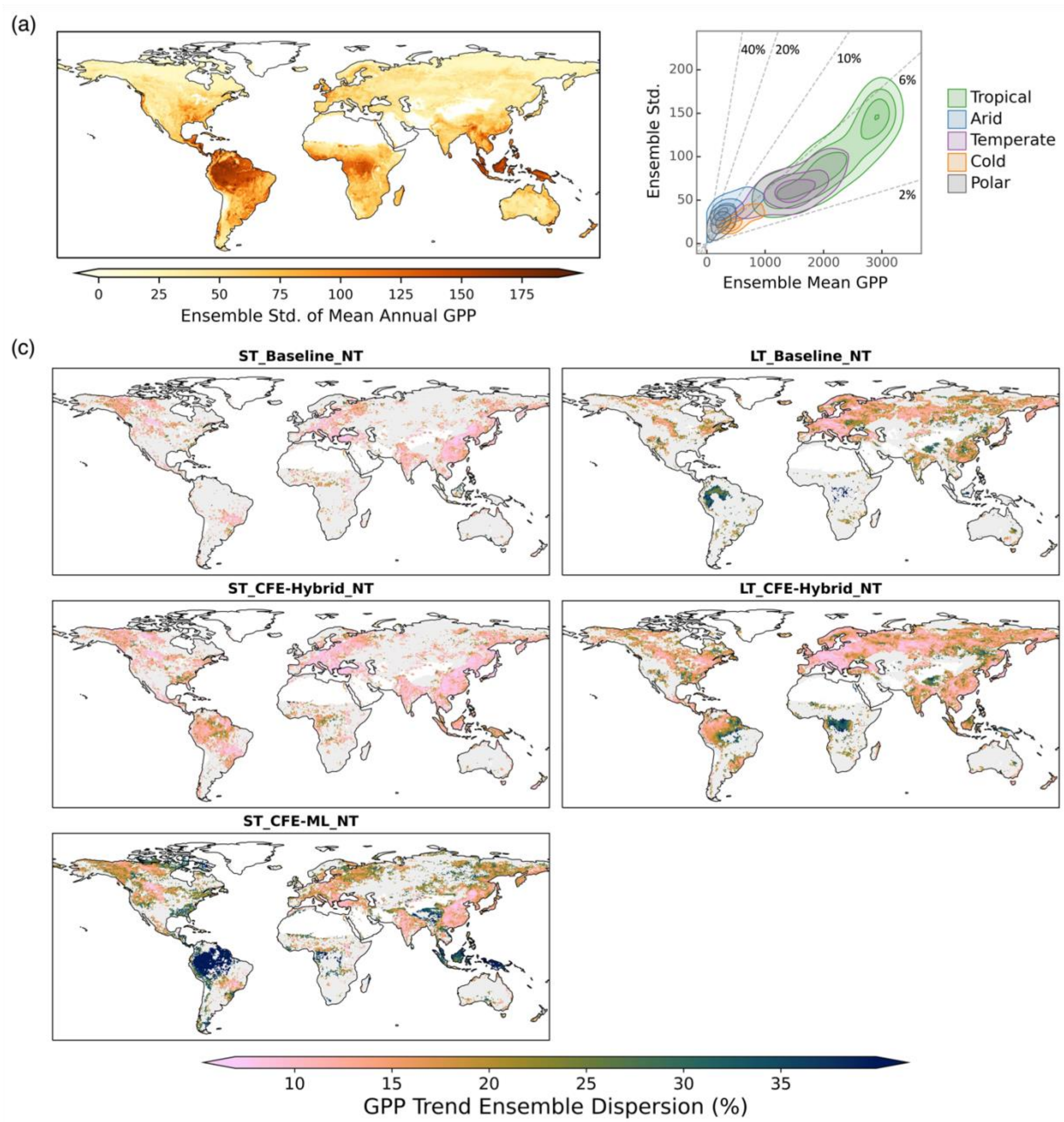

Figure 12. CEDAR-GPP estimation uncertainty derived from ensemble spread (standard deviation of 30 model predictions). (a) Spatial patterns of the absolute standard deviation from ensemble members in estimating the mean annual GPP from 2001 to 2018, using data from the ST_CFE-Hybrid_NT setup. (b) Relationships between ensemble standard deviation and ensemble mean in mean annual GPP. Colored contours denote clusters of Koppen climate zones. Dashed lines indicate the ratio between the ensemble standard deviation and the ensemble mean with values shown in percentage. (c) Spatial patterns of model uncertainty in GPP long-term trend estimation. Only areas where 90% of the ensemble members showed a statistically significant trend ($p<0.05$) are shown in the maps. The trend for the short-term datasets

(left column) was computed between 2001 to 2018. The trend for the long-term datasets (right column) was computed between 1982 to 2018.

4. Discussion

4.1 Uncertainties in GPP upscaling

Uncertainties in CEDAR-GPP estimations primarily stem from three components of the machine learning upscaling framework: eddy covariance GPP measurements, input satellite and climate datasets, and the machine learning model itself. Here we examine the three sources of uncertainties, discuss our strategies to reduce their impact, and assess the ability of our model ensemble spread indicator to indicate these uncertainties.

4.1.1 Eddy covariance data

Measurement and modeling errors inherent in eddy covariance GPP can propagate through the upscaling process. While random measurement errors in monthly GPP are typically very small due to error cancellation through temporal aggregation from the half-hourly data, systematic biases may be introduced by the partitioning approach used to derive GPP from the Net Ecosystem Exchange (NEE) measurements, which could be specific to certain environmental conditions (Keenan et al., 2019; Pastorello et al., 2020). This uncertainty was evidenced by a discrepancy between the CEDAR-GPP NT and DT setups. The mean annual GPP from the DT setup was slightly higher than that from the NT setup (Figure 6), and the DT setup also predicted a higher GPP trend in the long-term dataset (Figure 11). Notably, these discrepancies were relatively small compared to the predominant spatiotemporal patterns. Nevertheless, separate DT and NT setups in CEDAR-GPP offered an interesting quantification of the associated uncertainties over space and time, providing insights for future improvements of GPP partitioning approaches.

The heavily skewed representativeness of the eddy covariance data remains a key challenge in upscaling, a limitation well-documented in previous studies (Jung et al., 2020). Effective generalization in machine learning models requires a substantial volume of training data that adequately represents and balances unseen conditions. However, the geographical and temporal limitations of eddy covariance data introduce both systematic and random uncertainties in upscaled GPP estimations. Flux sites are primarily clustered in North America and Western Europe, with sparse availability in critical carbon exchange hotspots such as tropical, subtropical, and boreal regions (Figure 1). Consequently, estimated GPP from upscaling was commonly believed to carry high uncertainties in these areas. However, previous studies have found that humid tropical regions were associated with low extrapolation uncertainty despite the limited amount of flux sites (Jung et al., 2020). A pioneering study employing synthetic datasets from a deterministic terrestrial biosphere model assessed the generalizability of the upscaling approach (Jung et al., 2009). Results indicated that a machine learning model trained with data from the FLUXNET sites' location and times could account for 92% variation of GPP globally. Therefore, to fully understand the upscaling uncertainty, it is essential to carefully evaluate the generalization or extrapolation errors within the predictor space, which indicates the actual environmental controls and mechanisms of the ecosystem carbon fluxes (van der Horst et al., 2019; Villarreal and Vargas, 2021).

We compiled a large (~18000 site-months) set of high-quality eddy covariance data in generating CEDAR-GPP to potentially mitigate uncertainties associated with eddy covariance measurements. The FLUXNET2015 dataset was complemented by two regional networks processed under the same ONEFLUX protocol with additional sites and longer records. Data were screened with stringent quality control criteria to reduce measurement uncertainties. Nevertheless, uncertainties in GPP upscaling due to limited eddy covariance data representation remain substantial. Additionally, our analysis suggested that the estimated global GPP magnitudes were related to the eddy covariance GPP data used in the model. Global GPP magnitudes derived from CEDAR-GPP and FLUXSAT aligned closely with that from Terrestrial Biosphere Models (Anav et al., 2015), while FLUXCOM's estimation was much lower (Figure 6, Figure 11). FLUXSAT used FLUXNET2015 as the training set, which largely overlapped with that included in CEDAR-GPP (Joiner and Yoshida, 2020). FLUXCOM utilized the FLUXNET La Thuile set combined with CarboAfrica network, which consisted of a very different set of sites, with flux data processed with a different pipeline (Tramontana et al., 2016). The influence from the predictor datasets was minimal since all three datasets relied on MODIS-derived products. For a comprehensive evaluation of the impacts of flux site representativeness on upscaling, future research directions could include conducting synthetic experiments with simulations of ensembles of terrestrial biosphere models.

4.1.2 Input predictors and controlling factors

Input predictors, including satellite and climate datasets, bring additional uncertainties to upscaled GPP. First, satellite remote sensing data contains noises resulting from atmospheric conditions, sun-earth geometry, soil background, and geolocation inaccuracies. The models or algorithms used for variable estimation, such as those for retrieving LAI, fAPAR, LST, and soil moisture, also contain random errors and systematic biases specific to certain regions, biome types, or climatic conditions (Yan et al., 2016b; Fang et al., 2019; Ma et al., 2019). Additionally, satellite observations frequently contain missing values due to clouds, aerosols, snow, and satellite revisit cycles, leading to both systematic and random uncertainties. In producing CEDAR-GPP, we aimed to mitigate these uncertainties through comprehensive preprocessing procedures. Our temporal gap-filling strategy improved upon previous upscaling efforts by exploiting both the temporal dependency of vegetation status and long-term climatology, to reduce biases from missing values. Temporal and spatial aggregation further diminished the remaining data gaps and random noises. Nevertheless, it was still likely that considerable uncertainties remained in satellite datasets and propagated into the upscaled estimations.

The mismatch between the footprint of the eddy covariance measurements and the coarse resolution of satellite observations presents another significant, and potentially more impactful, source of uncertainties. Flux towers typically have a footprint of around ~1 km^2 (Chu et al., 2021), whereas satellite observations employed in CEDAR-GPP and most other upscaled datasets were at 5 km or lower resolution. Systematic and random errors could be introduced due to this mismatch, particularly in heterogenous biomes and areas with a mixture of vegetation and non-vegetated land covers. Gaber et al. (in prep) discovered that machine learning models trained with MODIS datasets at their native 500m resolution substantially outperformed those trained with aggregated datasets at 0.05-degree resolution, especially in capturing interannual variabilities. One approach to mitigate this issue is by generating upscaled datasets at a higher spatial resolution (e.g. 500m). Alternatively, models could be trained at a high resolution and applied to the coarse resolution to reduce computation and storage requirements (Dannenberg et al., 2023). However, this approach does not address inherent scaling errors in coarse-resolution satellite images (Yan et al., 2016a; Dong et al., 2023).

Besides the quality of predictors, successful machine learning upscaling also depends on a comprehensive set of features representing all controlling factors. Satellite-derived vegetation structural indicators have been found to be the most influential features in GPP upscaling (Tramontana et al., 2015); consequently, trends and interannual variabilities in upscaled GPP reflected that from the underlying vegetation structural datasets. For example, the FLUXCOM-RSv006 dataset was generated based on the MODIS collection 6 dataset, showing similar temporal dynamics globally as CEDAR-GPP and FLUXSAT. However, the previous version that utilized

MODIS collection 5 products exhibited minimal interannual variability and insignificant trend (Ryu et al., 2019).

Furthermore, information about resource limitations and stress factors can be crucial for certain biomes and/or under specific conditions (Stocker et al., 2018). For example, Dannenberg et al. (2023) found that incorporating LST from MODIS and soil moisture from the SMAP satellite datasets improved the machine learning estimation accuracy of GPP in drylands from $R^2 \sim 0.4$ to 0.7 for dryland sites in North America. CEDAR-GPP integrated multi-source satellite observations (optical, thermal, microwave) as well as climate variables to obtain comprehensive information about GPP dynamics. Nevertheless, as was commonly observed in machine learning upscaling, the models failed to capture interannual anomalies. This could imply that vital information for GPP estimation remained missing or inadequately represented in existing datasets. Examples include factors related to agricultural management practices (crop type, cultivar, irrigation, fertilization), plant hydraulic and physiological properties, as well as root and soil characteristics.

4.1.3 Machine learning models and uncertainty quantification

The choice of machine learning models and their parameterization has been found to have a relatively minor impact on the upscaling of GPP (Tramontana et al., 2015). CEDAR used the state-of-the-art boosting algorithm, XGBoost, which provided near-optimal performance considering the current data availability. Further reduction of model uncertainty will likely rely on additional information, such as increasing the number of training samples or incorporating more high-quality predictors. Additionally, temporal dependency of carbon fluxes responses to atmospheric controls may also be exploited with specialized deep neural networks such as recurrent neural networks or transformers (Besnard et al., 2019; Ma and Liang, 2022).

A key challenge, however, is the quantification of uncertainties in machine learning upscaling (Reichstein et al., 2019). The limited availability of eddy covariance data hinders a comprehensive assessment of the extrapolation errors; consequently, metrics of predictive performance from cross-validation are inherently biased. CEDAR derived estimation uncertainty for each GPP prediction using bootstrapping model ensemble, which naturally mimics the biased sampling of flux tower locations. Notably, the choice of input climate reanalysis datasets could also induce systematic differences in GPP spatial and temporal patterns (Tramontana et al., 2015). The FLUXCOM product used model ensembles based on different reanalysis datasets to capture these uncertainties. Additionally, different satellite datasets of vegetation structural proxies, such as LAI, also exhibited significant discrepancies (Jiang et al., 2017). Thus, an ensemble approach combining site-level bootstrapping with multiple sources of input predictors could potentially provide a more comprehensive quantification of uncertainties. Future work may also explore Bayesian neural networks, which provide uncertainty along with predictions and, at the same time, present high predictive power comparable to ensemble tree-based algorithms (Ma et al., 2021).

4.2 Long-term GPP changes and CO_2 fertilization effect

CEDAR-GPP was constructed using a comprehensive set of climate variables and multi-source satellite observations, thus, encapsulating long-term GPP dynamics from both direct and indirect effects of climate controls. Particularly, CEDAR-GPP included the direct CO_2 fertilization effect, which has been shown to dominate the increasing trend of global GPP (Chen et al., 2022). Incorporating these effects substantially improved long-term trends of GPP from site to global scales (Figure 5, 10, 11). CEDAR's CFE-Hybrid setup offered a conservative estimation of the direct CO_2 effects by simulating the light-limited sensitivity on LUE for C3 plants (Walker et al., 2021). Nevertheless, the model did not account for the impacts of nutrient availability, which could potentially constrain CO_2 fertilization (Reich et al., 2014; Peñuelas et al., 2017; Terrer et al., 2019). Furthermore, the sensitivity of light-limited photosynthesis is a function of temperature, resulting in the most pronounced increasing trend in the tropics (Figure 10). Yet the model assumed a fixed ratio of leaf-internal to ambient CO_2, and thus did not include any responses to vapor pressure deficit.

The CFE-ML model adopted a data-driven approach to infer CO_2 effects directly from eddy covariance data. This strategy allowed the model to capture any physiological pathways of the CO_2 impact evidenced in the eddy covariance measurements, including the increases of the biochemical rates as well as enhancements in water use efficiency (Keenan et al., 2013). The model successfully detected a strong positive effect of CO_2 on eddy covariance measured GPP, consistent with previous studies based on process-based and statistical models (Fernández-Martínez et al., 2017; Ueyama et al., 2020; Chen et al., 2022). Notably, the CFE-ML model could have included the impacts of other factors that exhibit a strong temporal correlation with CO_2. For example, industrialization-induced increases in nitrogen deposition could synergistically boost GPP alongside CO_2 (O'Sullivan et al., 2019). Technological and management improvements in agriculture that contribute to a global boost of crop photosynthesis (Zeng et al., 2014), might also be indirectly reflected in the model estimates. As a result, the CFE-ML predicted a GPP trend that more closely aligned with eddy covariance observations, and the upscaled dataset also showed a globally higher trend than CFE-Hybrid (Figure 5; Figure 10). Nevertheless, spatial patterns of GPP trends from the CFE-ML aligned with that from CFE-Hybrid, reflecting a strong temperature dependency, implying that the effects of CO_2 likely remained the most significant factor. Additionally, the considerable ensemble spread in the CO_2 trends from the CFE-ML model (Figure 11, Figure 13) underscored a high level of uncertainty in the machine learning quantified CO_2 effects. Future work may exploit explainable machine learning and causal inference to investigate the underlying mechanisms of CO_2 effects.

5. Data availability

The CEDAR-GPP product, comprising ten GPP datasets, is available at zenodo (https://doi.org/10.5281/zenodo.8212707). These datasets were generated at a spatial resolution of 0.05° and monthly time steps. Each dataset includes an ensemble mean GPP and an ensemble standard deviation.

6. Summary and conclusions

We present the CEDAR-GPP product generated by upscaling global eddy covariance measurements with machine learning and a broad range of satellite and climate variables. CEDAR-GPP comprises four long-term datasets from 1982 to 2020 and six short-term datasets from 2001 to 2020. These datasets encompass three different configurations of the incorporation of direct CO_2 fertilization effects and two partitioning approaches to derive GPP from eddy covariance data. The machine learning models of CEDAR-GPP achieved high capability in predicting monthly GPP, its seasonal cycles, and spatial variability within the globally distributed eddy covariance sites, with cross-validated R^2 between 0.56 to 0.79. Short-term model setups consistently outperformed long-term models due to considerably more and higher-quality information from multi-source satellite observations.

CEDAR-GPP advances satellite-based GPP estimations, as the first upscaled dataset that considered the direct biochemical effects of elevated atmospheric CO_2 on photosynthesis, which is responsible for an increasing land carbon sink over the past decades. We showed that incorporating this effect in our CFE-ML and CFE-Hybrid models substantially improved the estimation of GPP trends at eddy covariance sites. Global patterns of long-term GPP trends in the CFE-ML setups showed a strong temperature dependency consistent with biophysical theories. Aside from the trend, global spatial and temporal GPP patterns from CEDAR generally aligned with other satellite-based GPP datasets.

In conclusion, CEDAR-GPP, informed by global eddy covariance measurements (~18000 site-months) and a broad range of multi-source remote sensing observations and climatic variables, offered a comprehensive representation of global GPP spatial and temporal dynamics over the past four decades. The different CO_2 fertilization configures integrated in CEDAR-GPP offer new opportunities for understanding global ecosystem photosynthesis's response to increases in atmospheric CO_2 along different pathways over space and time. CEDAR-GPP is expected to serve as a valuable tool for benchmarking process-based modeling and constraining the global carbon cycle.

Supplement

The supplement related to this article is available online.

Author contributions

T. K. and Y. K. conceptualized the study. Y. K. performed the formal analysis and generated the final product. Y. K., T. K., M. B., and M. G. contributed to the development and investigation of the research. Y. K., M. G., and X. L. contributed to data curation and processing. Y. K. prepared the manuscript with contributions from all co-authors. T. K. supervised the project.

Acknowledgments

We are grateful to Dr. Youngryel Ryu for providing the BESS_Rad dataset and Dr. Martin Jung for sharing the FLUXCOM-RS006 dataset. We also thank Dr. Muyi Li for sharing early versions of the PKU GIMMS NDVI4g and LAI4g datasets with us.

Financial support

This research was supported by the U.S. Department of Energy Office of Science Early Career Research Program award #DE-SC0021023 and a NASA Award 80NSSC21K1705. TFK acknowledges additional support from the LEMONTREE (Land Ecosystem Models based On New Theory, obseRvations and ExperimEnts) project, funded through the generosity of Eric and Wendy

Schmidt by recommendation of the Schmidt Futures programme and NASA award #80NSSC20K1801.

Reference

Anav, A., Friedlingstein, P., Beer, C., Ciais, P., Harper, A., Jones, C., Murray-Tortarolo, G., Papale, D., Parazoo, N. C., Peylin, P., Piao, S., Sitch, S., Viovy, N., Wiltshire, A., and Zhao, M.: Spatiotemporal patterns of terrestrial gross primary production: A review, Reviews of Geophysics, 1–34, https://doi.org/10.1002/2015RG000483.Received, 2015.

Badgley, G., Anderegg, L. D. L., Berry, J. A., and Field, C. B.: Terrestrial gross primary production: Using NIRV to scale from site to globe, Global Change Biology, 25, 3731–3740, https://doi.org/10.1111/gcb.14729, 2019.

Baldocchi, D. D.: How eddy covariance flux measurements have contributed to our understanding of Global Change Biology, Global Change Biology, 26, 242–260, https://doi.org/10.1111/gcb.14807, 2020.

Beck, H. E., Zimmermann, N. E., McVicar, T. R., Vergopolan, N., Berg, A., and Wood, E. F.: Present and future köppen-geiger climate classification maps at 1-km resolution, Scientific Data, 5, 1–12, https://doi.org/10.1038/sdata.2018.214, 2018.

Beer, C., Reichstein, M., Tomelleri, E., Ciais, P., Jung, M., Carvalhais, N., Rödenbeck, C., Arain, M. A., Baldocchi, D., Bonan, G. B., Bondeau, A., Cescatti, A., Lasslop, G., Lindroth, A., Lomas, M., Luyssaert, S., Margolis, H., Oleson, K. W., Roupsard, O., Veenendaal, E., Viovy, N., Williams, C., Woodward, F. I., and Papale, D.: Terrestrial gross carbon dioxide uptake: Global distribution and covariation with climate, Science, 329, 834–838, https://doi.org/10.1126/science.1184984, 2010.

Berdugo, M., Gaitán, J. J., Delgado-Baquerizo, M., Crowther, T. W., and Dakos, V.: Prevalence and drivers of abrupt vegetation shifts in global drylands, Proceedings of the National Academy of Sciences, 119, e2123393119, https://doi.org/10.1073/pnas.2123393119, 2022.

Besnard, S., Carvalhais, N., Altaf Arain, M., Black, A., Brede, B., Buchmann, N., Chen, J., Clevers, J. G. P. W., Dutrieux, L. P., Gans, F., Herold, M., Jung, M., Kosugi, Y., Knohl, A., Law, B. E., Paul-Limoges, E., Lohila, A., Merbold, L., Roupsard, O., Valentini, R., Wolf, S., Zhang, X., and Reichstein, M.: Memory effects of climate and vegetation affecting net ecosystem CO2 fluxes in global forests, PLoS ONE, 14, 1–22, https://doi.org/10.1371/journal.pone.0211510, 2019.

Bloomfield, K. J., Stocker, B. D., Keenan, T. F., and Prentice, I. C.: Environmental controls on the light use efficiency of terrestrial gross primary production, Global Change Biology, 29, 1037–1053, https://doi.org/10.1111/gcb.16511, 2023.

Campbell, J. E., Berry, J. A., Seibt, U., Smith, S. J., Montzka, S. A., Launois, T., Belviso, S., Bopp, L., and Laine, M.: Large historical growth in global terrestrial gross primary production, Nature, 544, 84–87, https://doi.org/10.1038/nature22030, 2017.

Camps-Valls, G., Campos-Taberner, M., Moreno-Martínez, Á., Walther, S., Duveiller, G., Cescatti, A., Mahecha, M. D., Muñoz-Marí, J., García-Haro, F. J., Guanter, L., Jung, M., Gamon, J. A., Reichstein, M., and Running, S. W.: A unified vegetation index for quantifying the terrestrial biosphere, Science Advances, 7, eabc7447, https://doi.org/10.1126/sciadv.abc7447, 2021.

Cao, S., Li, M., Zhu, Z., Zha, J., Zhao, W., Duanmu, Z., Chen, J., Zheng, Y., and Chen, Y.: Spatiotemporally consistent global dataset of the GIMMS Leaf Area Index (GIMMS LAI4g) from 1982 to 2020, Earth System Science Data Discussions, 1–31, https://doi.org/10.5194/essd-2023-68, 2023.

Chen, C., Park, T., Wang, X., Piao, S., Xu, B., Chaturvedi, R. K., Fuchs, R., Brovkin, V., Ciais, P., Fensholt, R., Tømmervik, H., Bala, G., Zhu, Z., Nemani, R. R., and Myneni, R. B.: China and

India lead in greening of the world through land-use management, Nature Sustainability, 2, 122–129, https://doi.org/10.1038/s41893-019-0220-7, 2019.

Chen, C., Riley, W. J., Prentice, I. C., and Keenan, T. F.: CO2 fertilization of terrestrial photosynthesis inferred from site to global scales, Proceedings of the National Academy of Sciences, 119, 1–8, https://doi.org/10.1073/pnas.2115627119/-/DCSupplemental.Published, 2022.

Chen, T. and Guestrin, C.: XGBoost: a scalable tree boosting system, in: Proceedings of the 22nd ACM SIGKDD International Conference on Knowledge Discovery and Data Mining - KDD '16, 785–794, https://doi.org/10.1145/2939672.2939785, 2016.

Chu, H., Luo, X., Ouyang, Z., Chan, W. S., Dengel, S., Biraud, S. C., Torn, M. S., Metzger, S., Kumar, J., Arain, M. A., Arkebauer, T. J., Baldocchi, D., Bernacchi, C., Billesbach, D., Black, T. A., Blanken, P. D., Bohrer, G., Bracho, R., Brown, S., Brunsell, N. A., Chen, J., Chen, X., Clark, K., Desai, A. R., Duman, T., Durden, D., Fares, S., Forbrich, I., Gamon, J. A., Gough, C. M., Griffis, T., Helbig, M., Hollinger, D., Humphreys, E., Ikawa, H., Iwata, H., Ju, Y., Knowles, J. F., Knox, S. H., Kobayashi, H., Kolb, T., Law, B., Lee, X., Litvak, M., Liu, H., Munger, J. W., Noormets, A., Novick, K., Oberbauer, S. F., Oechel, W., Oikawa, P., Papuga, S. A., Pendall, E., Prajapati, P., Prueger, J., Quinton, W. L., Richardson, A. D., Russell, E. S., Scott, R. L., Starr, G., Staebler, R., Stoy, P. C., Stuart-Haëntjens, E., Sonnentag, O., Sullivan, R. C., Suyker, A., Ueyama, M., Vargas, R., Wood, J. D., and Zona, D.: Representativeness of Eddy-Covariance flux footprints for areas surrounding AmeriFlux sites, Agricultural and Forest Meteorology, 301–302, https://doi.org/10.1016/j.agrformet.2021.108350, 2021.

Dannenberg, M. P., Barnes, M. L., Smith, W. K., Johnston, M. R., Meerdink, S. K., Wang, X., Scott, R. L., and Biederman, J. A.: Upscaling dryland carbon and water fluxes with artificial neural networks of optical, thermal, and microwave satellite remote sensing, Biogeosciences, 20, 383–404, https://doi.org/10.5194/bg-20-383-2023, 2023.

De Kauwe, M. G., Medlyn, B. E., Zaehle, S., Walker, A. P., Dietze, M. C., Hickler, T., Jain, A. K., Luo, Y., Parton, W. J., Prentice, I. C., Smith, B., Thornton, P. E., Wang, S., Wang, Y.-P., Wårlind, D., Weng, E., Crous, K. Y., Ellsworth, D. S., Hanson, P. J., Seok Kim, H.-, Warren, J. M., Oren, R., and Norby, R. J.: Forest water use and water use efficiency at elevated CO2: a model-data intercomparison at two contrasting temperate forest FACE sites, Global Change Biology, 19, 1759–1779, https://doi.org/10.1111/gcb.12164, 2013.

De Kauwe, M. G., Keenan, T. F., Medlyn, B. E., Prentice, I. C., and Terrer, C.: Satellite based estimates underestimate the effect of CO2 fertilization on net primary productivity, Nature Climate Change, 6, 892–893, https://doi.org/10.1038/nclimate3105, 2016.

Dong, Y., Li, J., Jiao, Z., Liu, Q., Zhao, J., Xu, B., Zhang, H., Zhang, Z., Liu, C., Knyazikhin, Y., and Myneni, R. B.: A Method for Retrieving Coarse-Resolution Leaf Area Index for Mixed Biomes Using a Mixed-Pixel Correction Factor, IEEE Transactions on Geoscience and Remote Sensing, 61, 1–17, https://doi.org/10.1109/TGRS.2023.3235949, 2023.

Dorigo, W., Wagner, W., Albergel, C., Albrecht, F., Balsamo, G., Brocca, L., Chung, D., Ertl, M., Forkel, M., Gruber, A., Haas, E., Hamer, P. D., Hirschi, M., Ikonen, J., de Jeu, R., Kidd, R., Lahoz, W., Liu, Y. Y., Miralles, D., Mistelbauer, T., Nicolai-Shaw, N., Parinussa, R., Pratola, C., Reimer, C., van der Schalie, R., Seneviratne, S. I., Smolander, T., and Lecomte, P.: ESA CCI Soil Moisture for improved Earth system understanding: State-of-the art and future directions, Remote Sensing of Environment, 203, 185–215, https://doi.org/10.1016/j.rse.2017.07.001, 2017.

Dorigo, W. A., Gruber, A., De Jeu, R. A. M., Wagner, W., Stacke, T., Loew, A., Albergel, C., Brocca, L., Chung, D., Parinussa, R. M., and Kidd, R.: Evaluation of the ESA CCI soil moisture product using ground-based observations, Remote Sensing of Environment, 162, https://doi.org/10.1016/j.rse.2014.07.023, 2015.

Ehlers, I., Augusti, A., Betson, T. R., Nilsson, M. B., Marshall, J. D., and Schleucher, J.: Detecting long-term metabolic shifts using isotopomers: CO2-driven suppression of photorespiration in C3 plants over the 20th century, Proceedings of the National Academy of Sciences, 112, 15585–15590, https://doi.org/10.1073/pnas.1504493112, 2015.

Fang, H., Baret, F., Plummer, S., and Schaepman‐Strub, G.: An overview of global leaf area index (LAI): Methods, products, validation, and applications, Reviews of Geophysics, 2018RG000608, https://doi.org/10.1029/2018RG000608, 2019.

Fernández-Martínez, M., Vicca, S., Janssens, I. A., Ciais, P., Obersteiner, M., Bartrons, M., Sardans, J., Verger, A., Canadell, J. G., Chevallier, F., Wang, X., Bernhofer, C., Curtis, P. S., Gianelle, D., Grünwald, T., Heinesch, B., Ibrom, A., Knohl, A., Laurila, T., Law, B. E., Limousin, J. M., Longdoz, B., Loustau, D., Mammarella, I., Matteucci, G., Monson, R. K., Montagnani, L., Moors, E. J., Munger, J. W., Papale, D., Piao, S. L., and Peñuelas, J.: Atmospheric deposition, CO2, and change in the land carbon sink, Sci Rep, 7, 9632, https://doi.org/10.1038/s41598-017-08755-8, 2017.

Friedl, M. and Sulla-Menashe, D.: MCD12Q1 MODIS/Terra+Aqua Land Cover Type Yearly L3 Global 500m SIN Grid V006 [Data set], NASA EOSDIS Land Processes DAAC, https://doi.org/10.5067/MODIS/MCD12Q1.006, 2019.

Friedlingstein, P., Meinshausen, M., Arora, V. K., Jones, C. D., Anav, A., Liddicoat, S. K., and Knutti, R.: Uncertainties in CMIP5 climate projections due to carbon cycle feedbacks, Journal of Climate, 27, 511–526, https://doi.org/10.1175/JCLI-D-12-00579.1, 2014.

Friedlingstein, P., O'Sullivan, M., Jones, M. W., Andrew, R. M., Gregor, L., Hauck, J., Le Quéré, C., Luijkx, I. T., Olsen, A., Peters, G. P., Peters, W., Pongratz, J., Schwingshackl, C., Sitch, S., Canadell, J. G., Ciais, P., Jackson, R. B., Alin, S. R., Alkama, R., Arneth, A., Arora, V. K., Bates, N. R., Becker, M., Bellouin, N., Bittig, H. C., Bopp, L., Chevallier, F., Chini, L. P., Cronin, M., Evans, W., Falk, S., Feely, R. A., Gasser, T., Gehlen, M., Gkritzalis, T., Gloege, L., Grassi, G., Gruber, N., Gürses, Ö., Harris, I., Hefner, M., Houghton, R. A., Hurtt, G. C., Iida, Y., Ilyina, T., Jain, A. K., Jersild, A., Kadono, K., Kato, E., Kennedy, D., Klein Goldewijk, K., Knauer, J., Korsbakken, J. I., Landschützer, P., Lefèvre, N., Lindsay, K., Liu, J., Liu, Z., Marland, G., Mayot, N., McGrath, M. J., Metzl, N., Monacci, N. M., Munro, D. R., Nakaoka, S.-I., Niwa, Y., O'Brien, K., Ono, T., Palmer, P. I., Pan, N., Pierrot, D., Pocock, K., Poulter, B., Resplandy, L., Robertson, E., Rödenbeck, C., Rodriguez, C., Rosan, T. M., Schwinger, J., Séférian, R., Shutler, J. D., Skjelvan, I., Steinhoff, T., Sun, Q., Sutton, A. J., Sweeney, C., Takao, S., Tanhua, T., Tans, P. P., Tian, X., Tian, H., Tilbrook, B., Tsujino, H., Tubiello, F., van der Werf, G. R., Walker, A. P., Wanninkhof, R., Whitehead, C., Willstrand Wranne, A., et al.: Global Carbon Budget 2022, Earth System Science Data, 14, 4811–4900, 2023.

Gampe, D., Zscheischler, J., Reichstein, M., Sullivan, M. O., Smith, W. K., Sitch, S., and Buermann, W.: Increasing impact of warm droughts on northern ecosystem productivity over recent decades, Nature Climate Change, https://doi.org/10.1038/s41558-021-01112-8, 2021.

Gao, B. C.: NDWI - A normalized difference water index for remote sensing of vegetation liquid water from space, Remote Sensing of Environment, 58, 257–266, https://doi.org/10.1016/S0034-4257(96)00067-3, 1996.

Gitelson, A. A.: Remote estimation of leaf area index and green leaf biomass in maize canopies, Geophysical Research Letters, 30, 1248, https://doi.org/10.1029/2002GL016450, 2003.

Gruber, A., Scanlon, T., Van Der Schalie, R., Wagner, W., and Dorigo, W.: Evolution of the ESA CCI Soil Moisture climate data records and their underlying merging methodology, Earth System Science Data, 11, 717–739, https://doi.org/10.5194/essd-11-717-2019, 2019.

Haverd, V., Smith, B., Canadell, J. G., Cuntz, M., Mikaloff-Fletcher, S., Farquhar, G., Woodgate, W., Briggs, P. R., and Trudinger, C. M.: Higher than expected CO2 fertilization inferred from leaf to global observations, Global Change Biology, 26, 2390–2402, https://doi.org/10.1111/gcb.14950, 2020.

van der Horst, S. V. J., Pitman, A. J., De Kauwe, M. G., Ukkola, A., Abramowitz, G., and Isaac, P.: How representative are FLUXNET measurements of surface fluxes during temperature extremes?, Biogeosciences, 16, 1829–1844, https://doi.org/10.5194/bg-16-1829-2019, 2019.

Jiang, C., Ryu, Y., Fang, H., Myneni, R., Claverie, M., and Zhu, Z.: Inconsistencies of interannual variability and trends in long-term satellite leaf area index products, Global Change Biology, 23, 4133–4146, https://doi.org/10.1111/gcb.13787, 2017.

Joiner, J. and Yoshida, Y.: Satellite-based reflectances capture large fraction of variability in global gross primary production (GPP) at weekly time scales, Agricultural and Forest Meteorology, 291, 108092, https://doi.org/10.1016/j.agrformet.2020.108092, 2020.

Jung, M., Reichstein, M., and Bondeau, A.: Towards global empirical upscaling of FLUXNET eddy covariance observations: Validation of a model tree ensemble approach using a biosphere model, Biogeosciences, 6, 2001–2013, https://doi.org/10.5194/bg-6-2001-2009, 2009.

Jung, M., Reichstein, M., Margolis, H. A., Cescatti, A., Richardson, A. D., Arain, M. A., Arneth, A., Bernhofer, C., Bonal, D., Chen, J., Gianelle, D., Gobron, N., Kiely, G., Kutsch, W., Lasslop, G., Law, B. E., Lindroth, A., Merbold, L., Montagnani, L., Moors, E. J., Papale, D., Sottocornola, M., Vaccari, F., and Williams, C.: Global patterns of land-atmosphere fluxes of carbon dioxide , latent heat , and sensible heat derived from eddy covariance , satellite , and meteorological observations, Journal of Geophysical Research: Biogeosciences, 116, 1–16, https://doi.org/10.1029/2010JG001566, 2011.

Jung, M., Reichstein, M., Schwalm, C. R., Huntingford, C., Sitch, S., Ahlström, A., Arneth, A., Camps-Valls, G., Ciais, P., Friedlingstein, P., Gans, F., Ichii, K., Jain, A. K., Kato, E., Papale, D., Poulter, B., Raduly, B., Rödenbeck, C., Tramontana, G., Viovy, N., Wang, Y. P., Weber, U., Zaehle, S., and Zeng, N.: Compensatory water effects link yearly global land CO 2 sink changes to temperature, Nature, 541, 516–520, https://doi.org/10.1038/nature20780, 2017.

Jung, M., Schwalm, C., Migliavacca, M., Walther, S., Camps-Valls, G., Koirala, S., Anthoni, P., Besnard, S., Bodesheim, P., Carvalhais, N., Chevallier, F., Gans, F., S Goll, D., Haverd, V., Köhler, P., Ichii, K., K Jain, A., Liu, J., Lombardozzi, D., E M S Nabel, J., A Nelson, J., O'Sullivan, M., Pallandt, M., Papale, D., Peters, W., Pongratz, J., Rödenbeck, C., Sitch, S., Tramontana, G., Walker, A., Weber, U., and Reichstein, M.: Scaling carbon fluxes from eddy covariance sites to globe: Synthesis and evaluation of the FLUXCOM approach, Biogeosciences, 17, 1343–1365, https://doi.org/10.5194/bg-17-1343-2020, 2020.

Kang, Y., Ozdogan, M., Zhu, X., Ye, Z., Hain, C., and Anderson, M.: Comparative assessment of environmental variables and machine learning algorithms for maize yield prediction in the US Midwest, Environmental Research Letters, 15, https://doi.org/10.1088/1748-9326/ab7df9, 2020.

Keeling, R. F., Graven, H. D., Welp, L. R., Resplandy, L., Bi, J., Piper, S. C., Sun, Y., Bollenbacher, A., and Meijer, H. A. J.: Atmospheric evidence for a global secular increase in carbon isotopic discrimination of land photosynthesis, Proceedings of the National Academy of Sciences of the United States of America, 114, 10361–10366, https://doi.org/10.1073/pnas.1619240114, 2017.

Keenan, T. F. and Williams, C. A.: The terrestrial carbon sink, Annual Review of Environment and Resources, 43, 219–243, https://doi.org/10.1146/annurev-environ-102017-030204, 2018.
Keenan, T. F., Hollinger, D. Y., Bohrer, G., Dragoni, D., Munger, J. W., Schmid, H. P., and Richardson, A. D.: Increase in forest water-use efficiency as atmospheric carbon dioxide concentrations rise, Nature, 499, 324–327, https://doi.org/10.1038/nature12291, 2013.
Keenan, T. F., Prentice, I. C., Canadell, J. G., Williams, C. A., Wang, H., Raupach, M., and Collatz, G. J.: Recent pause in the growth rate of atmospheric CO2 due to enhanced terrestrial carbon uptake, Nature Communications, 7, 1–9, https://doi.org/10.1038/ncomms13428, 2016.
Keenan, T. F., Migliavacca, M., Papale, D., Baldocchi, D., Reichstein, M., Torn, M., and Wutzler, T.: Widespread inhibition of daytime ecosystem respiration, Nature Ecology and Evolution, 3, 407–415, https://doi.org/10.1038/s41559-019-0809-2, 2019.
Li, M., Cao, S., and Zhu, Z.: Spatiotemporally consistent global dataset of the GIMMS Normalized Difference Vegetation Index (PKU GIMMS NDVI) from 1982 to 2020, Earth System Science Data Discussions, 1–31, https://doi.org/10.5194/essd-2023-1, 2023.
Ma, H. and Liang, S.: Development of the GLASS 250-m leaf area index product (version 6) from MODIS data using the bidirectional LSTM deep learning model, Remote Sensing of Environment, 273, 112985, https://doi.org/10.1016/j.rse.2022.112985, 2022.
Ma, H., Zeng, J., Chen, N., Zhang, X., Cosh, M. H., and Wang, W.: Satellite surface soil moisture from SMAP, SMOS, AMSR2 and ESA CCI: A comprehensive assessment using global ground-based observations, Remote Sensing of Environment, 231, 111215, https://doi.org/10.1016/j.rse.2019.111215, 2019.
Ma, Y., Zhang, Z., Kang, Y., and Özdoğan, M.: Corn yield prediction and uncertainty analysis based on remotely sensed variables using a Bayesian neural network approach, Remote Sensing of Environment, 259, 112408, https://doi.org/10.1016/j.rse.2021.112408, 2021.
Myneni, R., Knyazikhin, Y., and Park, T.: MCD15A3H MODIS/Terra+Aqua Leaf Area Index/FPAR 4-day L4 Global 500m SIN Grid V006 [Data set], NASA EOSDIS Land Processes DAAC., https://doi.org/10.5067/MODIS/MCD15A3H.006, 2015a.
Myneni, R., Knyazikhin, Y., and Park, T.: MOD15A2H MODIS/Terra Leaf Area Index/FPAR 8-Day L4 Global 500m SIN Grid V006 [Data set], NASA EOSDIS Land Processes DAAC, https://doi.org/10.5067/MODIS/MOD15A2H.006, 2015b.
O'Sullivan, M., Spracklen, D. V., Batterman, S. A., Arnold, S. R., Gloor, M., and Buermann, W.: Have Synergies Between Nitrogen Deposition and Atmospheric CO 2 Driven the Recent Enhancement of the Terrestrial Carbon Sink?, Global Biogeochemical Cycles, 33, 163–180, https://doi.org/10.1029/2018GB005922, 2019.
O'Sullivan, M., Smith, W. K., Sitch, S., Friedlingstein, P., Arora, V. K., Haverd, V., Jain, A. K., Kato, E., Kautz, M., Lombardozzi, D., Nabel, J. E. M. S., Tian, H., Vuichard, N., Wiltshire, A., Zhu, D., and Buermann, W.: Climate-Driven Variability and Trends in Plant Productivity Over Recent Decades Based on Three Global Products, Global Biogeochemical Cycles, 34, https://doi.org/10.1029/2020GB006613, 2020.
Pastorello, G., Trotta, C., Canfora, E., Chu, H., Christianson, D., Cheah, Y. W., Poindexter, C., Chen, J., Elbashandy, A., Humphrey, M., Isaac, P., Polidori, D., Ribeca, A., van Ingen, C., Zhang, L., Amiro, B., Ammann, C., Arain, M. A., Ardö, J., Arkebauer, T., Arndt, S. K., Arriga, N., Aubinet, M., Aurela, M., Baldocchi, D., Barr, A., Beamesderfer, E., Marchesini, L. B., Bergeron, O., Beringer, J., Bernhofer, C., Berveiller, D., Billesbach, D., Black, T. A., Blanken, P. D., Bohrer, G., Boike, J., Bolstad, P. V., Bonal, D., Bonnefond, J. M., Bowling, D. R., Bracho, R., Brodeur, J., Brümmer, C., Buchmann, N., Burban, B., Burns, S. P., Buysse, P., Cale, P., Cavagna, M., Cellier, P., Chen, S., Chini, I., Christensen, T. R., Cleverly, J., Collalti, A., Consalvo, C., Cook, B. D., Cook, D., Coursolle, C., Cremonese, E., Curtis, P. S., D'Andrea, E., da Rocha, H., Dai, X., Davis,

K. J., De Cinti, B., de Grandcourt, A., De Ligne, A., De Oliveira, R. C., Delpierre, N., Desai, A. R., Di Bella, C. M., di Tommasi, P., Dolman, H., Domingo, F., Dong, G., Dore, S., Duce, P., Dufrêne, E., Dunn, A., Dušek, J., Eamus, D., Eichelmann, U., ElKhidir, H. A. M., Eugster, W., Ewenz, C. M., Ewers, B., Famulari, D., Fares, S., Feigenwinter, I., Feitz, A., Fensholt, R., Filippa, G., Fischer, M., Frank, J., Galvagno, M., Gharun, M., Gianelle, D., et al.: The FLUXNET2015 dataset and the ONEFlux processing pipeline for eddy covariance data, Scientific data, 7, 225, https://doi.org/10.1038/s41597-020-0534-3, 2020.

Peñuelas, J., Ciais, P., Canadell, J. G., Janssens, I. A., Fernández-Martínez, M., Carnicer, J., Obersteiner, M., Piao, S., Vautard, R., and Sardans, J.: Shifting from a fertilization-dominated to a warming-dominated period, Nature Ecology and Evolution, 1, 1438–1445, https://doi.org/10.1038/s41559-017-0274-8, 2017.

Piao, S., Wang, X., Park, T., Chen, C., Lian, X., He, Y., Bjerke, J. W., Chen, A., Ciais, P., Tømmervik, H., Nemani, R. R., and Myneni, R. B.: Characteristics, drivers and feedbacks of global greening, Nature Reviews Earth and Environment, 1, 14–27, https://doi.org/10.1038/s43017-019-0001-x, 2020.

Reich, P. B., Hobbie, S. E., and Lee, T. D.: Plant growth enhancement by elevated CO2 eliminated by joint water and nitrogen limitation, Nature Geoscience, 7, 920–924, https://doi.org/10.1038/ngeo2284, 2014.

Reichstein, M., Camps-Valls, G., Stevens, B., Jung, M., Denzler, J., Carvalhais, N., and Prabhat: Deep learning and process understanding for data-driven Earth system science, Nature, 566, 195–204, https://doi.org/10.1038/s41586-019-0912-1, 2019.

Ruehr, S., Keenan, T. F., Williams, C., Zhou, Y., Lu, X., Bastos, A., Canadell, J. G., Prentice, I. C., Sitch, S., and Terrer, C.: Evidence and attribution of the enhanced land carbon sink, Nat Rev Earth Environ, 1–17, https://doi.org/10.1038/s43017-023-00456-3, 2023.

Running, S., Mu, Q., and Zhao, M.: MOD17A2H MODIS/Terra Gross Primary Productivity 8-Day L4 Global 500m SIN Grid V006, https://doi.org/10.5067/MODIS/MOD17A2H.006, 2015.

Ryu, Y., Jiang, C., Kobayashi, H., and Detto, M.: MODIS-derived global land products of shortwave radiation and diffuse and total photosynthetically active radiation at 5 km resolution from 2000, Remote Sensing of Environment, 204, 812–825, https://doi.org/10.1016/j.rse.2017.09.021, 2018.

Ryu, Y., Berry, J. A., and Baldocchi, D. D.: What is global photosynthesis? History, uncertainties and opportunities, Remote Sensing of Environment, 223, 95–114, https://doi.org/10.1016/j.rse.2019.01.016, 2019.

Sabater, J. M.: ERA5-Land monthly averaged data from 1981 to present., Copernicus Climate Change Service (C3S) Climate Data Store (CDS), https://doi.org/doi:10.24381/cds.68d2bb30, 2019.

Schaaf, C. and Wang, Z.: MCD43C4 MODIS/Terra+Aqua BRDF/Albedo Nadir BRDF-Adjusted Ref Daily L3 Global 0.05Deg CMG V006 [Data set], NASA EOSDIS Land Processes DAAC., https://doi.org/10.5067/MODIS/MCD43C4.006, 2015.

Schwalm, C. R., Anderegg, W. R. L., Michalak, A. M., Fisher, J. B., Biondi, F., Koch, G., Litvak, M., Ogle, K., Shaw, J. D., Wolf, A., Huntzinger, D. N., Schaefer, K., Cook, R., Wei, Y., Fang, Y., Hayes, D., Huang, M., Jain, A., and Tian, H.: Global patterns of drought recovery, Nature, 548, 202–205, https://doi.org/10.1038/nature23021, 2017.

Smith, W. K., Reed, S. C., Cleveland, C. C., Ballantyne, A. P., Anderegg, W. R. L., Wieder, W. R., Liu, Y. Y., and Running, S. W.: Large divergence of satellite and Earth system model estimates of global terrestrial CO2 fertilization, Nature Climate Change, 6, 306–310, https://doi.org/10.1038/nclimate2879, 2016.

Still, C. J., Berry, J. A., Collatz, G. J., and DeFries, R. S.: Global distribution of C3 and C4 vegetation: Carbon cycle implications, Global Biogeochemical Cycles, 17, https://doi.org/10.1029/2001gb001807, 2003.

Still, C. J., Berry, J. A., Collatz, G. J., and DeFries, R. S.: ISLSCP II C4 Vegetation Percentage, in: Hall, Forrest G., G. Collatz, B. Meeson, S. Los, E. Brown de Colstoun, and D. Landis (eds.). ISLSCP Initiative II Collection. Data set., http://dx.doi.org/10.3334/ORNLDAAC/932, 2009.

Stocker, B. D., Zscheischler, J., Keenan, T. F., Prentice, I. C., Peñuelas, J., and Seneviratne, S. I.: Quantifying soil moisture impacts on light use efficiency across biomes, New Phytologist, 218, 1430–1449, https://doi.org/10.1111/nph.15123, 2018.

Stocker, B. D., Zscheischler, J., Keenan, T. F., Prentice, I. C., Seneviratne, S. I., and Peñuelas, J.: Drought impacts on terrestrial primary production underestimated by satellite monitoring, Nature Geoscience, 12, 264–270, https://doi.org/10.1038/s41561-019-0318-6, 2019.

Terrer, C., Jackson, R. B., Prentice, I. C., Keenan, T. F., Kaiser, C., Vicca, S., Fisher, J. B., Reich, P. B., Stocker, B. D., Hungate, B. A., Peñuelas, J., McCallum, I., Soudzilovskaia, N. A., Cernusak, L. A., Talhelm, A. F., Van Sundert, K., Piao, S., Newton, P. C. D., Hovenden, M. J., Blumenthal, D. M., Liu, Y. Y., Müller, C., Winter, K., Field, C. B., Viechtbauer, W., Van Lissa, C. J., Hoosbeek, M. R., Watanabe, M., Koike, T., Leshyk, V. O., Polley, H. W., and Franklin, O.: Nitrogen and phosphorus constrain the CO2 fertilization of global plant biomass, Nature Climate Change, 9, 684–689, https://doi.org/10.1038/s41558-019-0545-2, 2019.

Thoning, K. W., Crotwell, A. M., and Mund, J. W.: Atmospheric Carbon Dioxide Dry Air Mole Fractions from continuous measurements at Mauna Loa, Hawaii, Barrow, Alaska, American Samoa and South Pole. 1973-2020, Version 2021-08-09, National Oceanic and Atmospheric Administration (NOAA), Global Monitoring Laboratory (GML), Boulder, Colorado, USA, https://doi.org/10.15138/yaf1-bk21, 2021.

Tramontana, G., Ichii, K., Camps-Valls, G., Tomelleri, E., and Papale, D.: Uncertainty analysis of gross primary production upscaling using Random Forests, remote sensing and eddy covariance data, Remote Sensing of Environment, 168, 360–373, https://doi.org/10.1016/j.rse.2015.07.015, 2015.

Tramontana, G., Jung, M., Schwalm, C. R., Ichii, K., Camps-Valls, G., Ráduly, B., Reichstein, M., Arain, M. A., Cescatti, A., Kiely, G., Merbold, L., Serrano-Ortiz, P., Sickert, S., Wolf, S., and Papale, D.: Predicting carbon dioxide and energy fluxes across global FLUXNET sites with regression algorithms, Biogeosciences, 13, 4291–4313, https://doi.org/10.5194/bg-13-4291-2016, 2016.

Ueyama, M., Ichii, K., Kobayashi, H., Kumagai, T., Beringer, J., Merbold, L., Euskirchen, E. S., Hirano, T., Marchesini, L. B., Baldocchi, D., Saitoh, T. M., Mizoguchi, Y., Ono, K., Kim, J., Varlagin, A., Kang, M., Shimizu, T., Kosugi, Y., Bret-Harte, M. S., Machimura, T., Matsuura, Y., Ohta, T., Takagi, K., Takanashi, S., and Yasuda, Y.: Inferring CO2 fertilization effect based on global monitoring land-atmosphere exchange with a theoretical model, Environmental Research Letters, 15, 84009, https://doi.org/10.1088/1748-9326/ab79e5, 2020.

Villarreal, S. and Vargas, R.: Representativeness of FLUXNET Sites Across Latin America, Journal of Geophysical Research: Biogeosciences, 126, e2020JG006090, https://doi.org/10.1029/2020JG006090, 2021.

Walker, A. P., De Kauwe, M. G., Bastos, A., Belmecheri, S., Georgiou, K., Keeling, R. F., McMahon, S. M., Medlyn, B. E., Moore, D. J. P., Norby, R. J., Zaehle, S., Anderson-Teixeira, K. J., Battipaglia, G., Brienen, R. J. W., Cabugao, K. G., Cailleret, M., Campbell, E., Canadell, J. G., Ciais, P., Craig, M. E., Ellsworth, D. S., Farquhar, G. D., Fatichi, S., Fisher, J. B., Frank, D. C., Graven, H., Gu, L., Haverd, V., Heilman, K., Heimann, M., Hungate, B. A., Iversen, C. M., Joos, F., Jiang, M., Keenan, T. F., Knauer, J., Körner, C., Leshyk, V. O., Leuzinger, S., Liu, Y., MacBean, N., Malhi, Y., McVicar, T. R., Penuelas, J., Pongratz, J., Powell, A. S., Riutta, T., Sabot, M. E. B., Schleucher, J., Sitch, S., Smith, W. K., Sulman, B., Taylor, B., Terrer, C., Torn, M. S., Treseder, K. K., Trugman, A. T., Trumbore, S. E., van Mantgem, P. J., Voelker, S. L., Whelan, M. E., and Zuidema, P. A.: Integrating the evidence for a terrestrial carbon sink caused by increasing atmospheric CO_2, New Phytologist, 229, 2413–2445, https://doi.org/10.1111/nph.16866, 2021.

Walther, S., Besnard, S., Nelson, J. A., El-madany, T. S., Migliavacca, M., Weber, U., Ermida, S. L., Brümmer, C., Schrader, F., Prokushkin, A. S., Panov, A. V., and Jung, M.: Technical note : A view from space on global flux towers by MODIS and Landsat : The FluxnetEO dataset, Biogeosciences Discussions, 2021.

Wan, Z., Hook, S., and Hulley, G.: MOD11A1 MODIS/Terra Land Surface Temperature/Emissivity Daily L3 Global 1km SIN Grid V006 [Data set], NASA EOSDIS Land Processes DAAC, https://doi.org/10.5067/MODIS/MOD11A1.006, 2015a.

Wan, Z., Hook, S., and Hulley, G.: MYD11A1 MODIS/Aqua Land Surface Temperature/Emissivity Daily L3 Global 1km SIN Grid V006 [Data set], NASA EOSDIS Land Processes DAAC, https://doi.org/10.5067/MODIS/MYD11A1.006, 2015b.

Warm Winter 2020 Team and ICOS Ecosystem Thematic Centre.: Warm Winter 2020 ecosystem eddy covariance flux product for 73 stations in FLUXNET-Archive format—release 2022-1 (Version 1.0), https://doi.org/10.18160/2G60-ZHAK, 2022.

Wenzel, S., Cox, P. M., Eyring, V., and Friedlingstein, P.: Projected land photosynthesis constrained by changes in the seasonal cycle of atmospheric CO_2, Nature, 538, 499–501, https://doi.org/10.1038/nature19772, 2016.

Xiao, J., Zhuang, Q., Baldocchi, D. D., Law, B. E., Richardson, A. D., Chen, J., Oren, R., Starr, G., Noormets, A., Ma, S., Verma, S. B., Wharton, S., Wofsy, S. C., Bolstad, P. V., Burns, S. P., Cook, D. R., Curtis, P. S., Drake, B. G., Falk, M., Fischer, M. L., Foster, D. R., Gu, L., Hadley, J. L., Hollinger, D. Y., Katul, G. G., Litvak, M., Martin, T. A., Matamala, R., McNulty, S., Meyers, T. P., Monson, R. K., Munger, J. W., Oechel, W. C., Paw U, K. T., Schmid, H. P., Scott, R. L., Sun, G., Suyker, A. E., and Torn, M. S.: Estimation of net ecosystem carbon exchange for the conterminous United States by combining MODIS and AmeriFlux data, Agricultural and Forest Meteorology, 148, 1827–1847, https://doi.org/10.1016/j.agrformet.2008.06.015, 2008.

Yan, K., Park, T., Yan, G., Chen, C., Yang, B., Liu, Z., Nemani, R. R., Knyazikhin, Y., and Myneni, R. B.: Evaluation of MODIS LAI/FPAR product collection 6. Part 1: Consistency and improvements, Remote Sensing, 8, 1–16, https://doi.org/10.3390/rs8050359, 2016a.

Yan, K., Park, T., Yan, G., Liu, Z., Yang, B., Chen, C., Nemani, R. R., Knyazikhin, Y., and Myneni, R. B.: Evaluation of MODIS LAI/FPAR product collection 6. Part 2: Validation and intercomparison, Remote Sensing, 8, 460, https://doi.org/10.3390/rs8060460, 2016b.

Yang, F., Ichii, K., White, M. A., Hashimoto, H., Michaelis, A. R., Votava, P., Zhu, A. X., Huete, A., Running, S. W., and Nemani, R. R.: Developing a continental-scale measure of gross primary production by combining MODIS and AmeriFlux data through Support Vector Machine approach, Remote Sensing of Environment, 110, 109–122, https://doi.org/10.1016/j.rse.2007.02.016, 2007.

Yang, R., Wang, J., Zeng, N., Sitch, S., Tang, W., McGrath, M. J., Cai, Q., Liu, D., Lombardozzi, D., Tian, H., Jain, A. K., and Han, P.: Divergent historical GPP trends among state-of-the-art multi-model simulations and satellite-based products, Earth System Dynamics, 13, 833–849, https://doi.org/10.5194/esd-13-833-2022, 2022.

Yuan, H., Dai, Y., Xiao, Z., Ji, D., and Shangguan, W.: Reprocessing the MODIS Leaf Area Index products for land surface and climate modelling, Remote Sensing of Environment, 115, 1171–1187, https://doi.org/10.1016/j.rse.2011.01.001, 2011.

Zeng, J., Matsunaga, T., Tan, Z.-H., Saigusa, N., Shirai, T., Tang, Y., Peng, S., and Fukuda, Y.: Global terrestrial carbon fluxes of 1999–2019 estimated by upscaling eddy covariance data with a random forest, Sci Data, 7, 313, https://doi.org/10.1038/s41597-020-00653-5, 2020.

Zeng, N., Zhao, F., Collatz, G. J., Kalnay, E., Salawitch, R. J., West, T. O., and Guanter, L.: Agricultural Green Revolution as a driver of increasing atmospheric CO2 seasonal amplitude, Nature, 515, 394–397, https://doi.org/10.1038/nature13893, 2014.

Zhang, Y.: A global spatially contiguous solar-induced fluorescence (CSIF) dataset using neural networks (2000-2020), National Tibetan Plateau Data Center, https://doi.org/10.11888/Ecolo.tpdc.271751., 2021.

Zhang, Y., Joiner, J., Hamed Alemohammad, S., Zhou, S., and Gentine, P.: A global spatially contiguous solar-induced fluorescence (CSIF) dataset using neural networks, Biogeosciences, 15, 5779–5800, https://doi.org/10.5194/bg-15-5779-2018, 2018.

Zheng, Y., Shen, R., Wang, Y., Li, X., Liu, S., Liang, S., Chen, J. M., Ju, W., Zhang, L., and Yuan, W.: Improved estimate of global gross primary production for reproducing its long-Term variation, 1982-2017, Earth System Science Data, 12, 2725–2746, https://doi.org/10.5194/essd-12-2725-2020, 2020.

Zhu, Z., Piao, S., Myneni, R. B., Huang, M., Zeng, Z., Canadell, J. G., Ciais, P., Sitch, S., Friedlingstein, P., Arneth, A., Cao, C., Cheng, L., Kato, E., Koven, C., Li, Y., Lian, X., Liu, Y., Liu, R., Mao, J., Pan, Y., Peng, S., Peuelas, J., Poulter, B., Pugh, T. A. M., Stocker, B. D., Viovy, N., Wang, X., Wang, Y., Xiao, Z., Yang, H., Zaehle, S., and Zeng, N.: Greening of the Earth and its drivers, Nature Climate Change, 6, 791–795, https://doi.org/10.1038/nclimate3004, 2016.

References

Automatic citation updates are disabled. To see the bibliography, click Refresh in the Zotero tab.